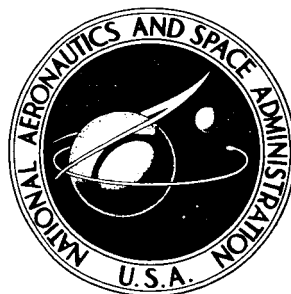


36P

8

N 63 21057  
Code 1

NASA TECHNICAL NOTE



NASA TN D-1956

OTS: \$1.00

NASA TN D-1956

**AERODYNAMIC DAMPING OF A  
0.02-SCALE SATURN SA-1 MODEL  
VIBRATING IN THE FIRST  
FREE-FREE BENDING MODE**

*by Perry W. Hanson and Robert V. Doggett, Jr.;  
Langley Research Center,  
Langley Station, Hampton, Va.*

TECHNICAL NOTE D-1956

AERODYNAMIC DAMPING OF A 0.02-SCALE SATURN SA-1 MODEL  
VIBRATING IN THE FIRST FREE-FREE BENDING MODE

By Perry W. Hanson and Robert V. Doggett, Jr.

Langley Research Center  
Langley Station, Hampton, Va.

NATIONAL AERONAUTICS AND SPACE ADMINISTRATION

NATIONAL AERONAUTICS AND SPACE ADMINISTRATION

---

TECHNICAL NOTE D-1956

---

AERODYNAMIC DAMPING OF A 0.02-SCALE SATURN SA-1 MODEL  
VIBRATING IN THE FIRST FREE-FREE BENDING MODE

By Perry W. Hanson and Robert V. Doggett, Jr.

*7 refs*

SUMMARY

The aerodynamic damping of a flexibly mounted 0.02-scale aeroelastic model of the Saturn SA-1 launch vehicle vibrating in the first free-free mode was measured at Mach numbers from 0.70 to 2.87 at several levels of dynamic pressure. Also investigated were two other configurations. One was the basic scaled model with rigid stabilizing fins added at the rear of the model, and the other configuration had, in addition to the fins, a winged spacecraft which replaced the nose cone of the scaled model.

An "electrical power-input" method was used to determine the damping of the configurations tested. The experimentally determined values are compared with some applicable theoretical results. The results of the investigation indicate that aerodynamic damping in the first free-free elastic vibration mode was small and stabilizing for all configurations tested.

Agreement of calculated aerodynamic damping derivatives with the experimental results was erratic. Good agreement was obtained between the experimental results and some empirical quasi-steady calculations based on static pressure distribution measurements made on a rigid model of similar geometry.

INTRODUCTION

The aerodynamics associated with elastic deformations of launch vehicles during the high dynamic pressure portion of their boost trajectories is playing an increasingly important role in determining the design requirements for stability and strength of the vehicles. Launch-vehicle structures are of necessity relatively flexible and can be subject to aeroelastic instabilities particularly in the cases where lifting spacecrafts are involved. The need for suitable theoretical approaches and experimental data on the oscillatory aerodynamic

derivatives of flexible slender bodies of revolution characteristic of launch vehicles has led to a research program oriented (1) to evaluate methods of handling these structural dynamics problems, (2) to provide a better understanding of the general nature of these problems, and (3) to provide design information for selected specific vehicles.

As part of this program, the feasibility of using flexible models to provide experimental data on the oscillatory aerodynamic damping characteristics of slender flexible bodies was investigated and the results reported in reference 1. These results indicated that aerodynamic damping on bodies of this type was very small. However, the model used in reference 1 was a simple smooth cylinder with a blunt conical nose. The question arises as to whether the technique could be extended to launch vehicles that have much more complicated shapes.

Therefore, the present investigation was undertaken to measure the oscillatory aerodynamic damping derivatives of a 0.02-scale aeroelastic model of the Saturn SA-1 launch vehicle. In addition, the effects of adding rigid fins and of adding fins and a winged spacecraft in place of the regular nose cone were investigated. The aerodynamic damping measurement technique used was essentially the electrical power-input method described in reference 1.

The tests were conducted in the Langley 8-foot transonic pressure tunnel over the Mach number range from 0.70 to 1.20 and in the Langley Unitary Plan wind tunnel over the Mach number range from 1.50 to 2.87.

Several theoretical approaches (refs. 2 to 7) were used to calculate predicted aerodynamic damping coefficients. Considerations used in applying the theories are presented in the appendix. The results are compared with the experimental results.

#### SYMBOLS

$A$	distribution function of damping portion of aerodynamic loading
$b(t)$	nose amplitude
$C_A$	generalized aerodynamic damping
$C_{cr}$	critical value of damping, $2M_S\omega$
$C_s$	structural damping
$C_h$	damping derivative, $2\mu k \frac{C_A}{C_{cr}}$
$c_{n\alpha}$	steady-state section normal-force-curve slope



$f_h$	frequency of first free-free bending mode
$f_\theta$	frequency of model rigid-body pitch mode
$H(x)$	mode shapes based on unit tip deflection of model center line
$I$	electrical current through shaker moving coils
$k$	reduced frequency, $\frac{\omega L}{V}$
$L$	length of basic model, 3.238 ft
$M_s$	generalized structural mass
$N_{Ma}$	free-stream Mach number
$P$	electrical power consumed by shaker moving coil circuit
$q$	dynamic pressure, $\frac{1}{2}\rho V^2$
$q_1, q_2$	proportionality constants in equation (1)
$Q_h^\bullet$	generalized force associated with aerodynamic damping
$R$	electrical resistance of shaker moving coil circuit
$r_m$	radius of model at rear, 0.217 ft
$r\left(\frac{x}{r_r}\right)$	nondimensional model radius at station $x$
$r_r$	reference radius (radius of cylinder enclosing scalloped portion of model, 0.214 ft)
$t$	time
$V$	free-stream velocity
$W$	total model weight
$x$	longitudinal coordinate measured from nose of basic model configuration, positive aft
$x_f$	longitudinal location of shaker applied sinusoidal force
$\gamma$	ratio of specific heats, air

$\theta$  angle between sloping portions of model surface and model undeflected center line in the vertical plane

$\rho$  test medium density

$\mu$  mass ratio, 
$$\frac{M_s}{\rho \pi r_r^2 L \int_0^{L/r_r} \left[ \frac{r \left( \frac{x}{r_r} \right)}{r_r} \right] H^2 \left( \frac{x}{r_r} \right) d \left( \frac{x}{r_r} \right)}$$

$\omega$  circular frequency

Subscripts:

M model properties

F full-scale vehicle properties

Dots over symbols indicate derivatives with respect to time.

## APPARATUS AND TEST PROCEDURE

### Model and Support System

General dimensions of the three model configurations tested are presented in figure 1. The basic model configuration was a 0.02-geometric-scale aeroelastic model of the Saturn SA-1 launch vehicle at a particular point in its boost trajectory. The fins are a 0.02 geometric scale of a proposed fin configuration for a later Saturn vehicle. The winged spacecraft has a scaled wing area and shape that approximates that of a proposed spacecraft. The dimensions of the fins and the winged spacecraft (which were not dynamically scaled) are presented in figures 2 and 3, respectively.

Scaling.— A point on the boost trajectory where the vehicle will be subjected to the highest dynamic pressures was chosen as the point at which the vehicle weight distribution would be scaled and flow conditions simulated. However, as the model neared completion it became apparent that the stiffness levels desired in the model were not being realized and the model stiffness and mass levels were altered to scale the full-scale vehicle at a Mach number slightly lower ( $N_{Ma} = 1.2$  instead of 1.3) and a weight condition slightly heavier ( $6.44 \times 10^5$  pounds instead of  $6.28 \times 10^5$  pounds) than originally anticipated. These revised full-scale vehicle properties and flow conditions are shown in table I along with the scaled values and the actual model properties and maximum model flow conditions at  $N_{Ma} = 1.2$ . An attempt was made to scale both mass and stiffness distribution only for the basic model. Also shown in the table are values of generalized mass and critical structural damping for all three model configurations, and the scaling relations used for the basic model configuration.

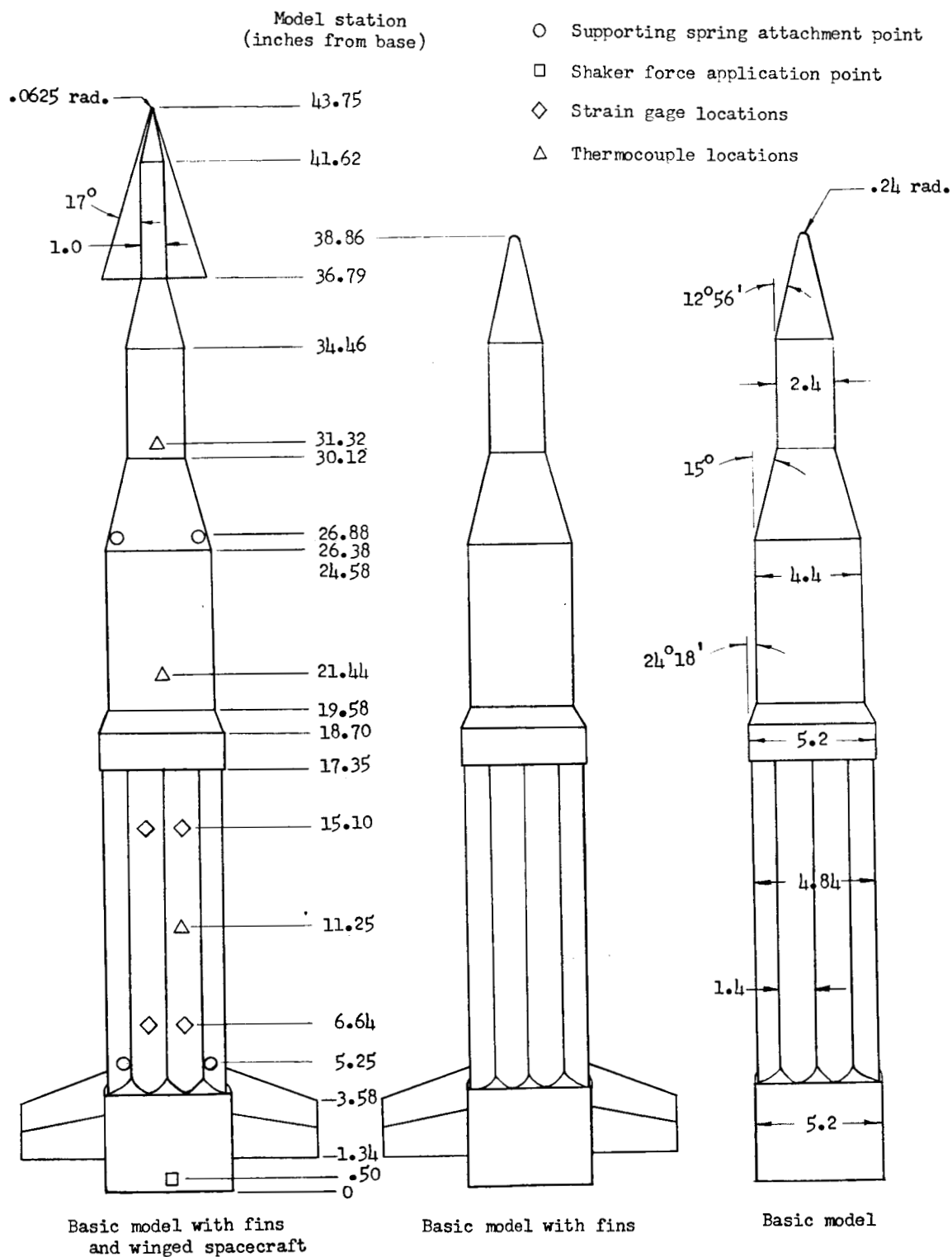


Figure 1.- Model geometry (plan view). All dimensions are in inches except as noted.

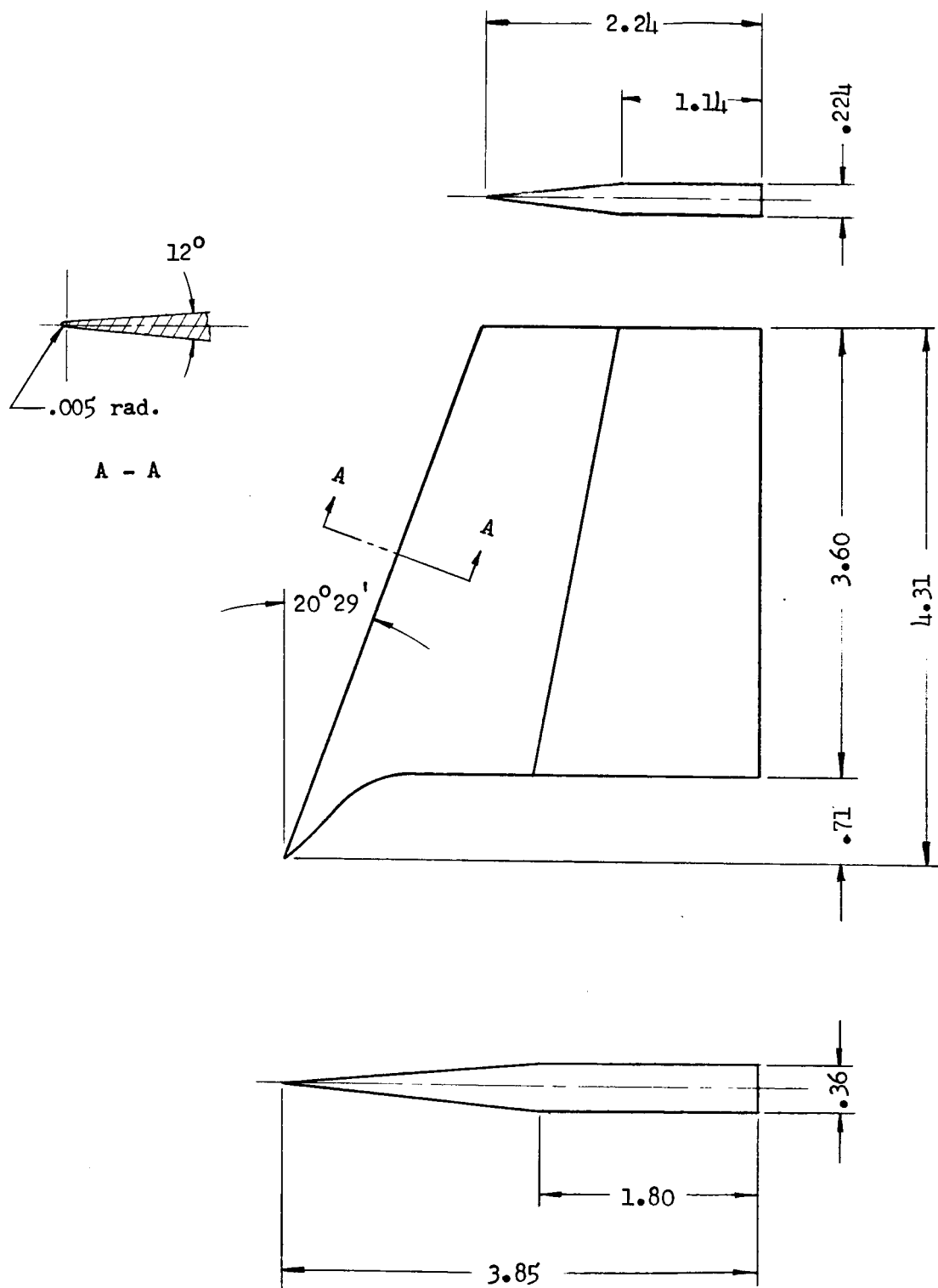


Figure 2.- Fin geometry. All dimensions are in inches except as noted.

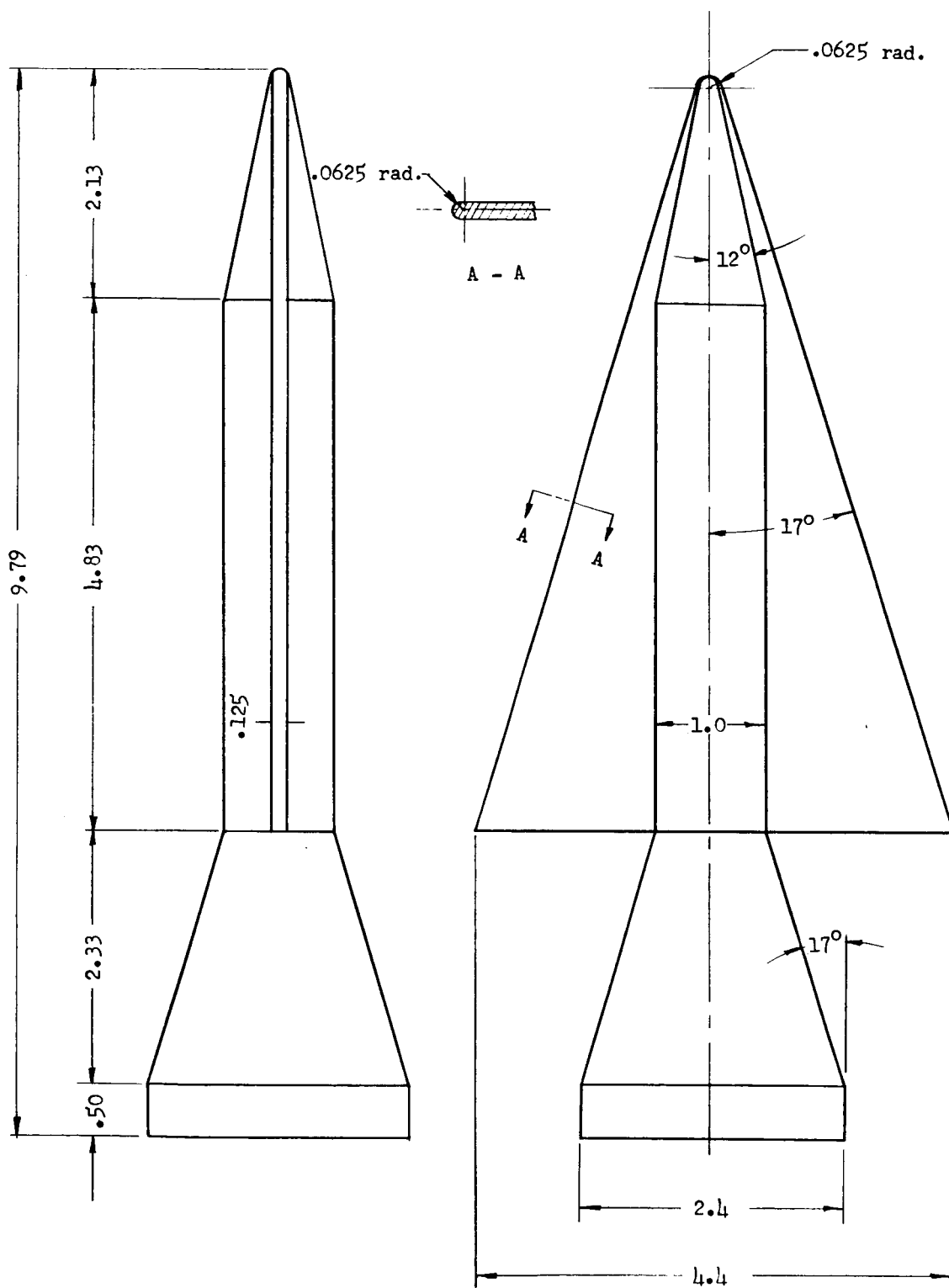


Figure 3.- Geometry of winged spacecraft. All dimensions are in inches except as noted.

TABLE I.- SCALING RELATIONS AND PHYSICAL PROPERTIES OF MODELS

Properties and flow conditions	Full-scale vehicle values	Scaled vehicle values (a)	Actual model properties and maximum flow conditions at $N_{Ma} = 1.2$		
			Basic model	Basic model with fins (b)	Basic model with fins and winged spacecraft (b)
$N_{Ma}$ . . . . .	1.2	1.2	1.2	1.2	1.2
$V$ , ft/sec . . . . .	1,200	1,255	1,255	1,255	1,255
$q$ , lb/sq ft . . . . .	670	1,100	1,250	1,250	500
$\rho$ , slugs/cu ft . . . .	$9.3 \times 10^{-4}$	$13.95 \times 10^{-4}$	$15.9 \times 10^{-4}$	$15.9 \times 10^{-4}$	$6.36 \times 10^{-4}$
$\rho V$ , lb-sec/cu ft : . .	1.12	1.75	1.96	1.96	0.67
$W$ , lb . . . . .	$6.44 \times 10^5$	7.73	7.78	8.07	8.22
Center of gravity, in. from rear . . . .	729	14.58	14.63	14.20	14.83
$f_h$ , cps . . . . .	2.9	151	153	148	118
$f_\theta$ , cps . . . . .	0.3	15.7	14.4	14.0	12.6
$M_s$ , slugs . . . . .	-----	-----	0.0305	0.0320	0.047
$C_{cr}$ , lb-sec/ft . . . .	-----	-----	58.4	59.4	69.5

<sup>a</sup>Scaling relations used:

$$\frac{L_M}{L_F} = 0.02$$

$$\frac{W_M}{W_F} = \left(\frac{L_M}{L_F}\right)^3 \left(\frac{\rho_M}{\rho_F}\right) = 12.0 \times 10^{-6}$$

$$\frac{V_M}{V_F} = 1.045$$

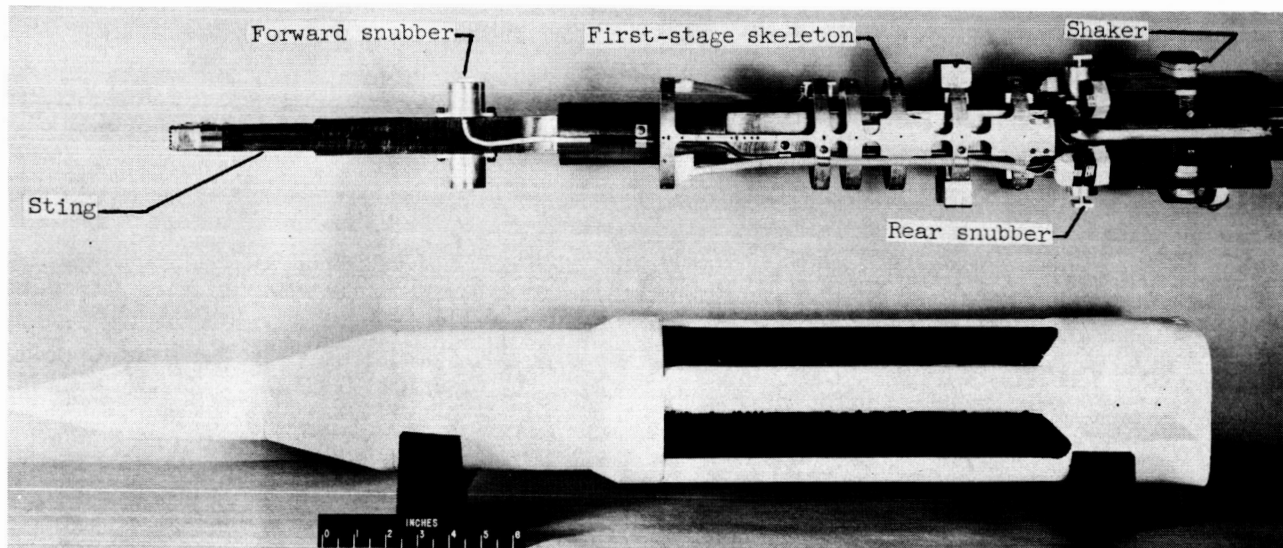
$$\frac{f_{h,M}}{f_{h,F}} = \left(\frac{L_F}{L_M}\right) \left(\frac{V_M}{V_F}\right) = 52.2$$

$$\frac{\rho_M}{\rho_F} = 1.50$$

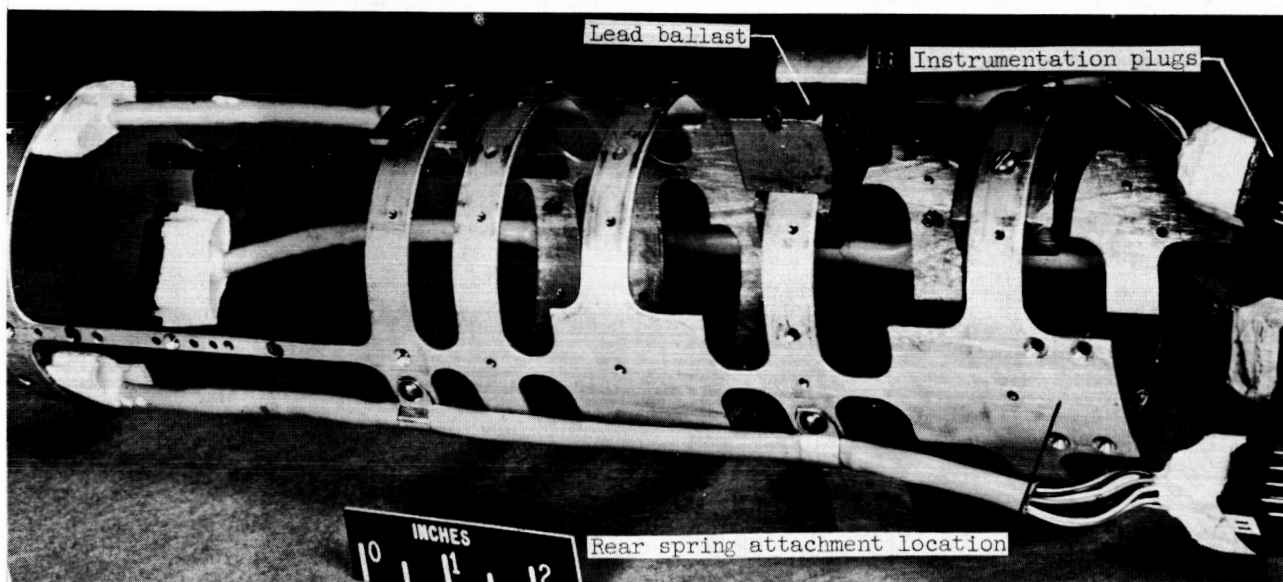
$$\frac{q_M}{q_F} = \left(\frac{\rho_M}{\rho_F}\right) \left(\frac{V_M}{V_F}\right)^2 = 1.64$$

<sup>b</sup>Fins and winged spacecraft are not elastically scaled components.

Construction.- Some of the details of model construction, the support system, and the method of model excitation are shown in the photographs of figure 4. The model skin was constructed of fiber glass, the thickness of which governed the stiffness along the model. Only a negligible amount of stiffness was contributed by the first-stage skeleton. The purpose of the skeleton was to stiffen the model radially and to provide attachment points for weights, instrumentation, and the rear mounting springs. In figure 4(a) the model skin or shell is shown assembled under the sting in the longitudinal position it would occupy on the sting. Shown mounted on the sting are the first-stage skeleton, the forward and rear model "snubbers" which were extended to physically restrain the model during starting and stopping transient flow conditions, and the electromagnetic shaker which was used to excite the models at their first free-free natural frequencies. A more detailed view of the first-stage skeleton, which was formed from an aluminum tube,



(a) Assembled model shell with first-stage skeleton and electromagnetic shaker on sting.

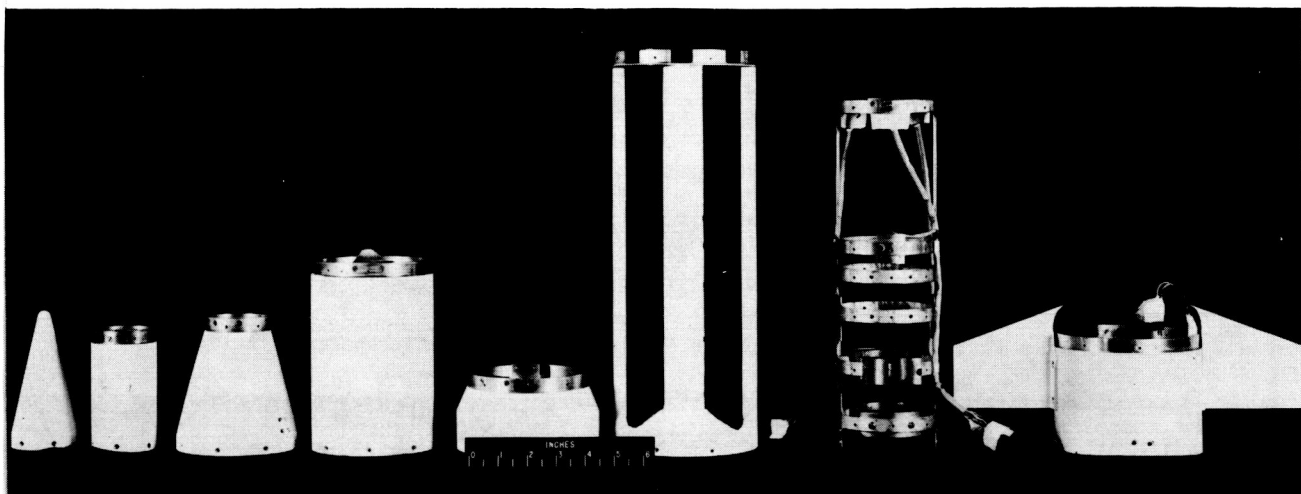


(b) Details of first-stage skeleton.

L-63-3195

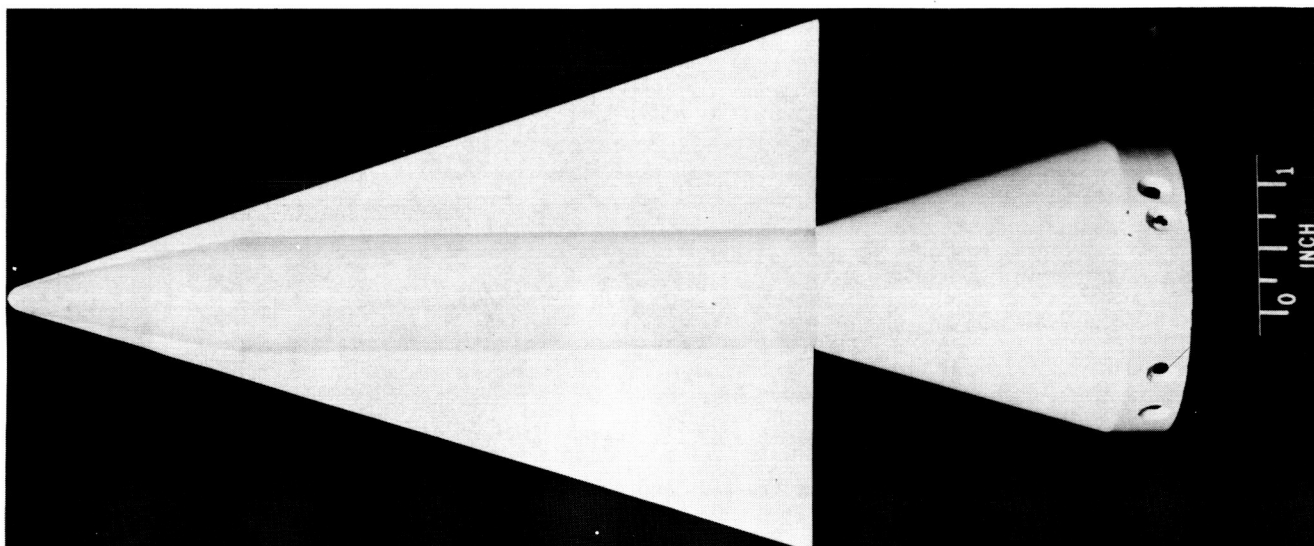
Figure 4.- Model construction and method of mounting and shaking.

is shown in figure 4(b). Also shown are some of the lead ballasts which were used to obtain the proper mass distribution. Figure 4(c) shows the model components disassembled except for the fins being attached to the shaker section of the model. Figure 4(d) is a photograph of the winged spacecraft. The fuselage and conical base were machined from aluminum and made hollow to decrease the weight. The wings are solid 1/8-inch-thick aluminum alloy. The model support system is shown in figures 4(e), 4(f), and 4(g). Figure 4(e) is a schematic diagram of the overall spring support system. The forward-support spring assembly



(c) Model component parts.

L-61-6022

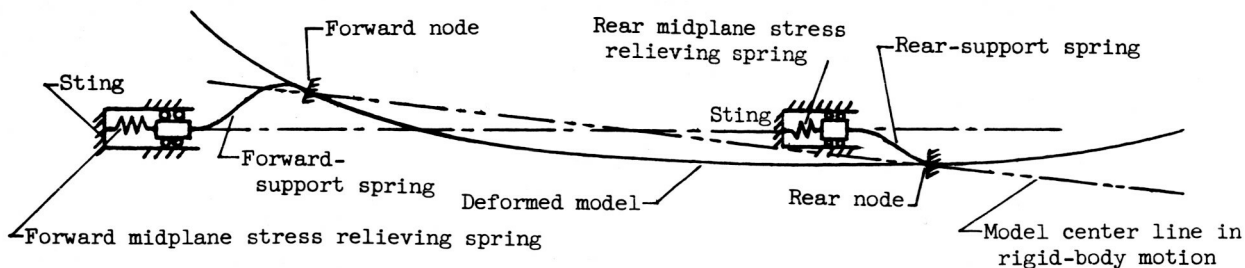


(d) Winged spacecraft.

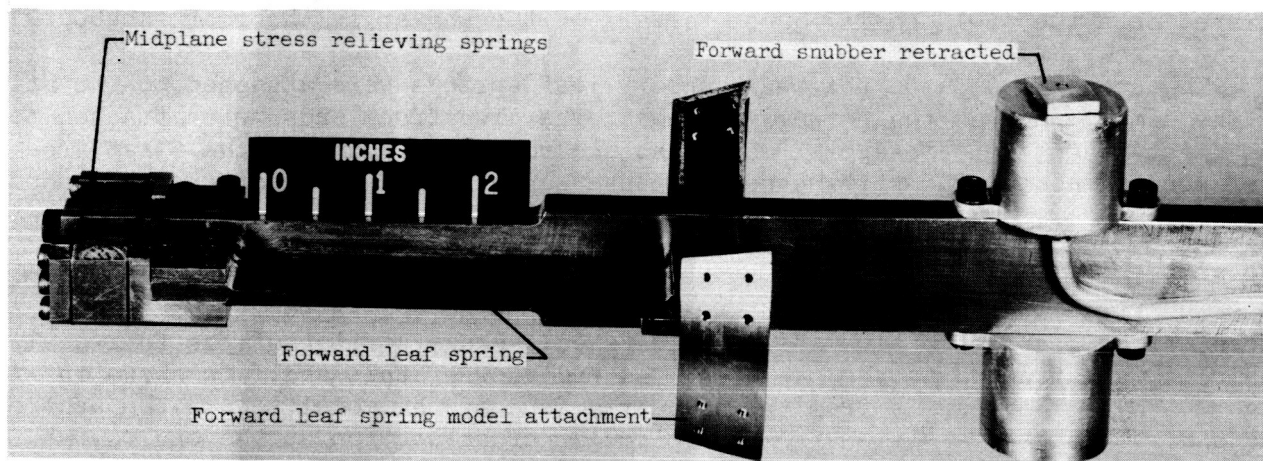
L-62-3820

Figure 4.- Continued.

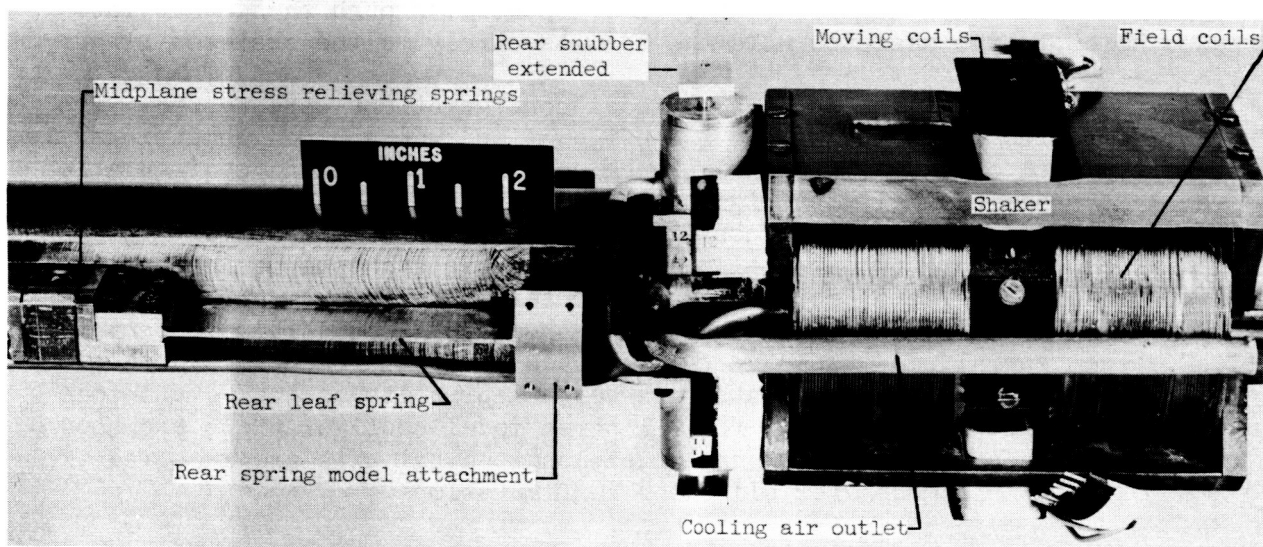




(e) Schematic diagram of spring support system.



(f) Forward-support spring assembly.



(g) Rear-support spring assembly and details of electromagnetic shaker. L-63-3196

Figure 4.- Continued.

is shown in detail in figure 4(f). The upstream end of the leaf spring is attached to the sting through a set of parallel transverse springs. These springs can move fore and aft as the leaf springs deflect. This arrangement alleviates midplane stresses in the leaf springs caused by "rigid-body" motions. The other ends of the leaf springs are attached to the model approximately at the first free-free bending mode forward node point.

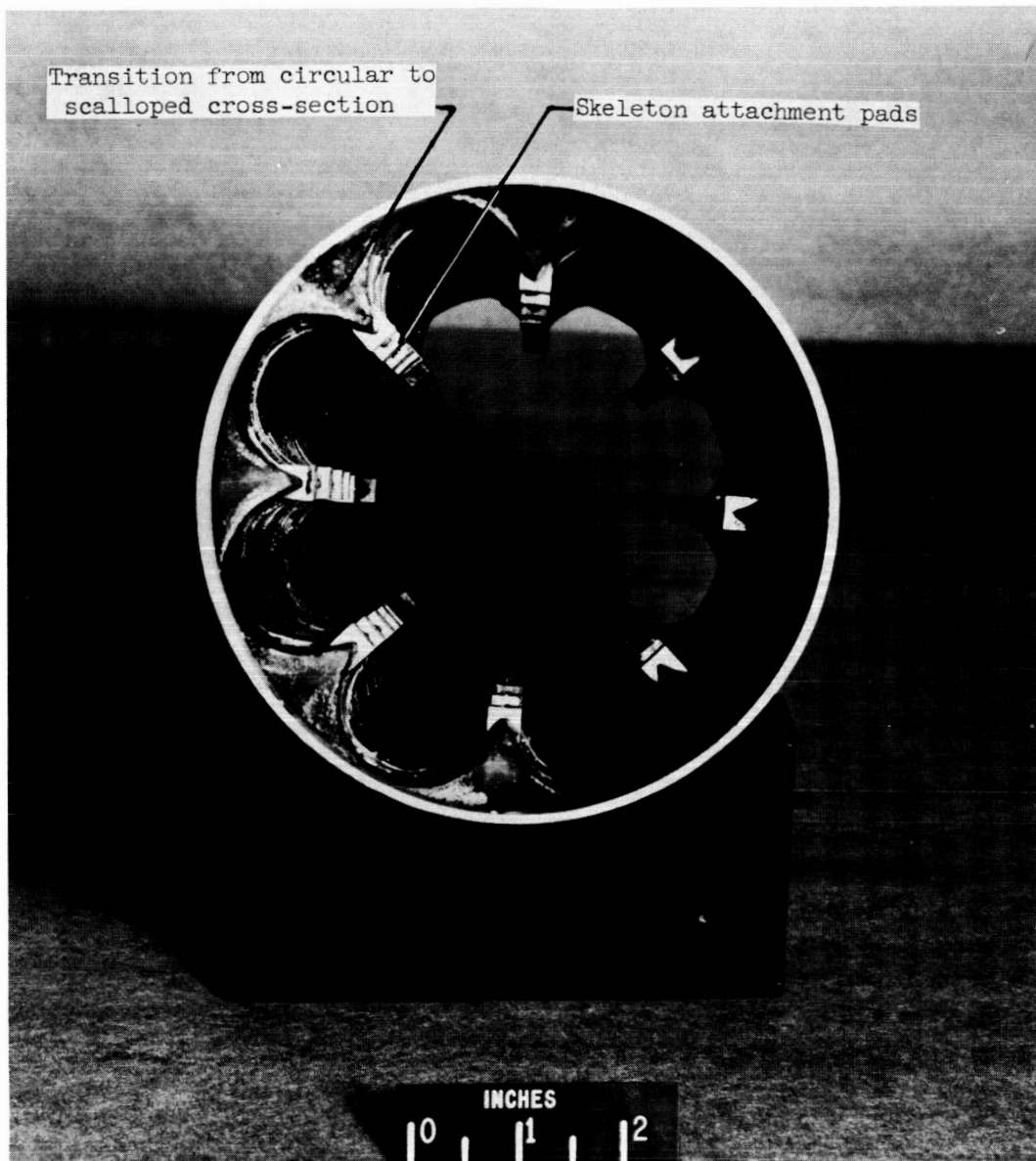
The electromagnetic shaker and rear-support spring assembly are shown in detail in figure 4(g). The stationary portion of the shaker (field coils and poles) was attached to the sting, whereas the armatures or moving coils were attached to the model. The tube shown extending along the field coils is perforated on the sides next to the coils. The shaker was cooled by forcing air down the inside of the sting and out into the perforated tubes from which it was sprayed onto the field coils. Just forward of the shaker is the rear "snubber."

The upstream ends of the rear-support leaf springs were attached to the sting in the same manner as the forward springs. The downstream ends were attached to the first-stage skeleton approximately at the rear node point of the first free-free bending mode. The stiffnesses of these support leaf springs were chosen so that the model would pitch about its center of gravity with a frequency that scaled that of the full-scale vehicle.

The first-stage shell (an integral piece of fiber glass that had a "scal-loped" cross section to simulate the clustered tankage portion of the full-scale vehicle) was attached to the skeleton. An end view of this shell is shown in figure 4(h). The view is from the downstream end of the model toward the upstream end and shows the transition from the circular cross section at the end to the scalloped cross section. Also shown are the skeleton mounting pads. These aluminum pads were machined to fit the contour of the scallops and were bonded to the fiber glass shell while it was being molded. Screws through these pads into threaded holes in the skeleton held the shell securely to the skeleton rings.

Model physical properties.- Three model configurations were tested. The first, referred to as the basic model configuration, was a 0.02-geometric-scale aeroelastic model of the Saturn SA-1 launch vehicle. The second configuration was merely the basic model with rigid fins added in the horizontal plane at the aft end of the model. The third configuration was the basic model with fins plus a rigid winged spacecraft that replaced the nose cone and some ballast weight on the basic model. The total model weights, centers of gravity, generalized masses, values of critical structural damping, and natural frequencies are presented in table I. The generalized masses were calculated from experimentally determined mass distributions (model components were weighed prior to assembly) and mode shapes. The weight distributions for all three model configurations are shown in table II. The positions along the model longitudinal axis are measured from the nose of the basic model for all three configurations.

The model mode shapes were determined by forcing the model with the electromagnetic shaker at the resonant frequency and measuring the variation along the model of the relative vertical displacement by means of a small velocity pickup. The first free-free bending mode shapes and natural frequencies for all three configurations are presented in figure 5. Also, the full-scale vehicle mode shape



(h) End view of first-stage shell.

L-61-6020.1

Figure 4.- Concluded.

(unpublished data from Marshall Space Flight Center) is compared with that of the basic model. It was planned that the investigation would cover free-free bending modes higher than the first but "hoop" modes (that involved deformations in cross sections) coupled with the higher bending modes and made any measurements in these modes of questionable value. Also, it was planned that the investigation would cover the rigid-body pitch mode of vibration but this mode coupled with sting motions so that the model could not be forced in a pure pitching motion.

TABLE II.- WEIGHT DISTRIBUTION

[x measured from nose of basic model, positive rearward; L = 3.238 ft]

x/L	Weight distribution, lb/in., for -		
	Basic model	Basic model with fins	Basic model with fins and winged spacecraft
-0.126	-----	-----	0
-.068	-----	-----	.0864
0	0	0	-----
.053	-----	-----	.0483
.113	.0258	.0258	.0217
.139	.8090	.8090	.4870
.153	.0143	.0143	.0143
.178	.2570	.2570	.2570
.212	.0143	.0143	.0143
.238	.1484	.1484	.1484
.305	.0156	.0156	.0156
.334	.5500	.5500	.5500
.381	.0210	.0210	.0210
.407	.6426	.6426	.6426
.483	.0210	.0210	.0210
.496	.3608	.3608	.3608
.541	.0500	.0500	.0500
.566	.3581	.3581	.3581
.685	.0638	.0638	.0638
.698	.2798	.2798	.2798
.711	.0638	.0638	.0638
.723	.1278	.1278	.1278
.741	.0638	.0638	.0638
.766	.7481	.7481	.7481
.791	.0638	.0638	.0638
.810	1.0960	1.0960	1.0960
.839	.0638	.0638	.0638
.865	1.3080	1.3080	1.3080
.894	.0638	.0638	.0638
.919	.2290	.3312	.3312
.966	-----	.1422	.1422
.974	.0400	.0400	.0400
1.000	.4412	.4412	.4412

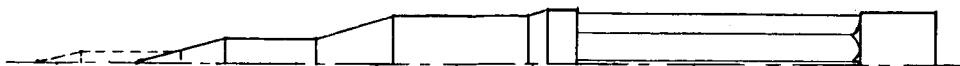
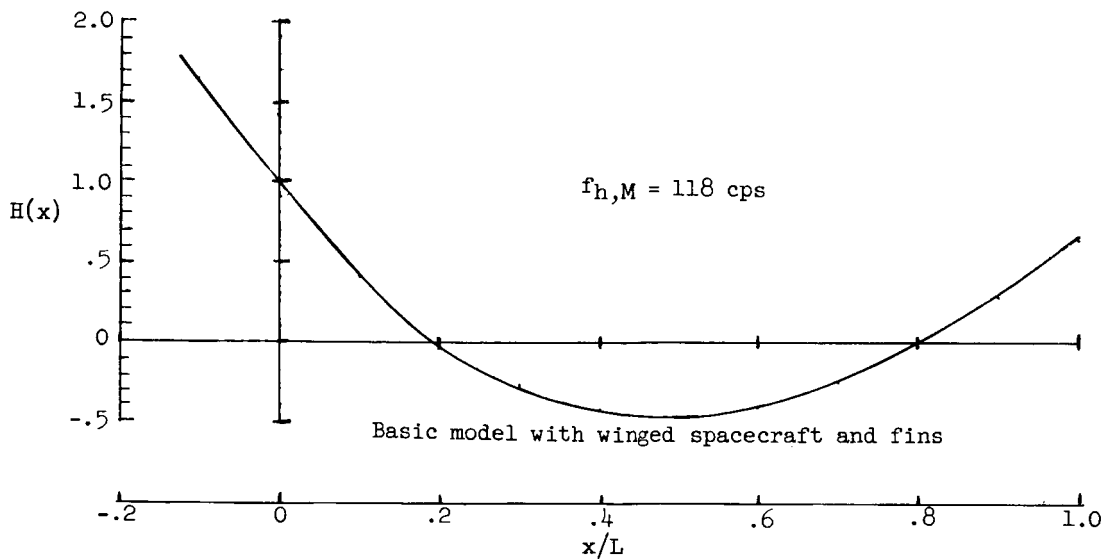
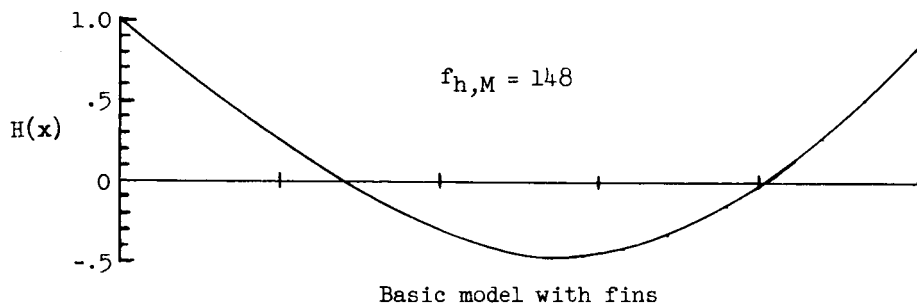
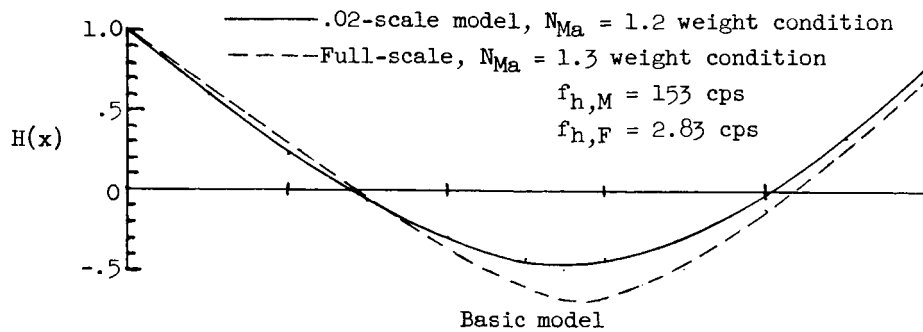


Figure 5.-- Mode shapes of configurations tested.

## Instrumentation

The model instrumentation consisted of three electrical wire resistance type strain gages bonded to the skin to monitor bending moments on the model and to indicate relative vibration amplitude and three skin thermocouples to indicate the skin temperature. The locations of these pickups on the basic model are shown in figure 1. Thermocouples also were imbedded in the moving coils and field coils of the shaker in order to provide a means for monitoring the coil temperatures.

A variable-frequency oscillator and power amplifier were used to provide alternating current to the shaker moving coils and a direct-current variable voltage power supply was used to provide direct current to the shaker field coils. A fouling light circuit provided a means of determining that the moving coils were riding free of the stationary parts of the shaker.

The readout instrumentation consisted of the following items:

(1) True root-mean-square vacuum tube voltmeter: indicated model vibration amplitude from strain gages

(2) True root-mean-square vacuum tube voltmeter: used across a precision 1-ohm resistor to indicate current applied to moving coils of shaker

(3) Direct-current ammeter: indicated current applied to field coils of shaker (held constant at 2.5 amps)

(4) Low-power-factor wattmeter: indicated power drawn by moving coils

(5) Oscilloscope: provided means for monitoring wave form of force output of shaker and of model response

(6) Electronic period counter: used to determine frequency of forced oscillations

(7) Recording potentiometer: indicated temperature of the model skin, the moving coils, and the field coils

(8) Electronic dampometer: measured the logarithmic decrement and was used to monitor the structural damping in order to determine any large changes due to structural failure

(9) Oscillograph: recorded signals from model instrumentation pickups

A block diagram of the instrumentation setup is shown in figure 6. The supplementary resistance measuring circuit was employed to determine accurately the resistance of the moving coils which varied because of temperature changes in the coils. Immediately after each test point, a battery-supplied voltage was applied to the coils and the voltage and corresponding current noted from the voltmeter and ammeter, respectively.

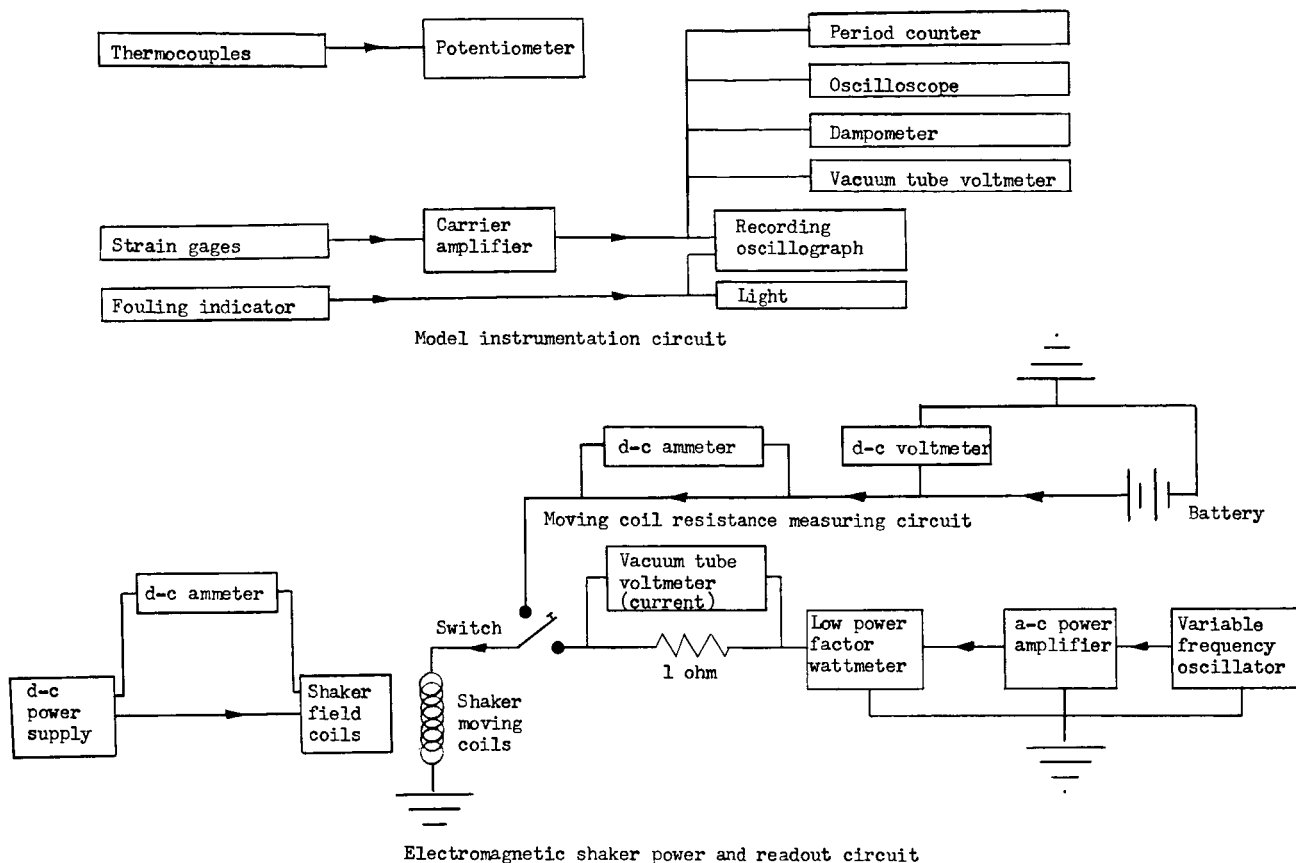


Figure 6.- Block diagram of shaker, model, and readout instrumentation.

## Wind Tunnels

The investigation was conducted in two wind tunnels. The Langley 8-foot transonic pressure tunnel was used for Mach numbers up to 1.2 and the Langley Unitary Plan wind tunnel was used for Mach numbers from 1.50 to 2.87. Both tunnels are of the continuous-flow type with variable Mach number and density control. Stagnation temperature in both tunnels was held constant at approximately 125° F.

## Test Procedure

Before the model was mounted on the sting, it was supported on soft rubber cords at the first free-free bending mode nodal points and its natural frequency determined. The model was then mounted on the sting via the support spring assemblies and shaken at its resonant frequency. No change in node points or frequency in the first free-free mode was detectable.

The test procedure used in both tunnels was essentially the same. After mounting the model in the tunnel it was shaken at the resonant frequency of the first free-free bending mode with no air flowing at several test-section

pressures from atmospheric down to moderately low vacuums, and with cooling air both on and off. No change in resonant frequency or damping was observed for any of these conditions. While the model was vibrating at a given amplitude, data necessary for application of the power-input method of determining damping were recorded. The power to the shaker was then abruptly shut off (and the shaker moving coils disconnected from the electrical circuit), the decaying oscillations of the model were recorded, and the logarithmic decrement was measured by the electronic dampometer. This device provided a quick means of detecting any extreme changes in structural damping due to structural failure, loose screws, and so forth. After obtaining the no-wind data, the model snubbers were extended and the tunnel started. When the tunnel reached the desired operating conditions the model snubbers were retracted and the above procedure repeated except that the decaying oscillations no longer produced a signal that was "clean" enough to permit the use of the dampometer. The process was continued at the various Mach numbers and at several levels of dynamic pressure at each Mach number. The Reynolds number range for the tests was from  $0.7 \times 10^6$  to  $1.5 \times 10^6$  based on a reference diameter of 0.428 feet.

#### DATA REDUCTION TECHNIQUE

Relationships for determining the ratio of damping to critical damping from the electrical measurements of the power-input method are developed in appendix A of reference 1. The resulting expression (eq. (A22) of ref. 1) is given as follows in the notation of the present paper:

$$\frac{C_A + C_S}{C_{cr}} = \frac{q_1^2 H(x_f)}{2q_2 M_s \omega} \frac{I^2}{P - I^2 R} \quad (1)$$

where

- $H(x_f)$  mode-shape deflection at shaker location
- $I$  current through shaker moving coils
- $M_s$  generalized mass of model
- $P$  electric power consumed by shaker moving coil circuit
- $q_1$  proportionality constant relating shaker force output to current applied to moving coils
- $q_2$  proportionality constant relating product of model nose velocity and applied force to power applied to moving coils
- $R$  electrical resistance of shaker moving coil circuit
- $\omega$  natural vibration frequency at test condition



The structural damping of the model configurations tested was found to be slightly dependent on amplitude of vibration and model skin temperature as was the case for the models tested in reference 1. In the present investigation all tests were made at the same amplitude level. However, since the model skin temperature could not be controlled it was necessary to construct calibration curves of structural damping ratio against skin temperature so that structural damping measured before the tests could be corrected to correspond to that associated with the skin temperature of the model at the test point. The temperature calibration curves used for the three configurations are shown in figure 7. The structural damping ratio is plotted against the model skin temperature as indicated by the thermocouple located 11.25 inches from the rear of the model. It was originally conceived that the average temperature indicated by the three thermocouples distributed along the model would be used; however, it was found that the changes of structural damping were much more sensitive to changes in temperature of the scalloped skin section of the model, particularly the portion where the model changes from a circular cross section to a scalloped cross section. Heat applied to this area alone changed the structural damping of the basic model over 10 times the change in damping produced when the front portions of the model were heated by the same amount. Thus, it is believed that using the temperature of the model in the vicinity of the most rearward thermocouple provided the most nearly correct indication of structural-damping change with temperature.

In order to obtain the aerodynamic damping from the total damping measured, the no-wind structural damping was adjusted to account for the difference in wind-off and wind-on structural damping due to model temperature changes. For convenience in presenting the data, an average value of the structural damping ratio was then added to the aerodynamic damping ratio for each test condition to give the total damping ratio that is presented in the results.

The ratios of aerodynamic damping to critical damping obtained in this manner apply only to the particular mechanical systems used in these tests. In order to make the damping measurements of more general value, a nondimensional damping force derivative  $C_h^*$  can be defined in terms of the usual flutter parameters, reduced frequency and mass ratio, in such a manner as to permit estimation of aerodynamic damping of similar configurations having somewhat different structural characteristics. Thus, from equation (A4)

$$\frac{C_A}{C_{cr}} = \frac{\pi \rho V r_r^2}{2 M_s \omega} \int_0^{L/r_r} c_{n\alpha} \left[ \frac{r(\frac{x}{r_r})}{r_r} \right] H^2 \left( \frac{x}{r_r} \right) d \left( \frac{x}{r_r} \right) \quad (2)$$

(For the configuration with the winged spacecraft, the lower limit of integration in eq. (2) and subsequent equations is from the winged spacecraft nose,  $\frac{x}{r_r} = -1.902$ .)

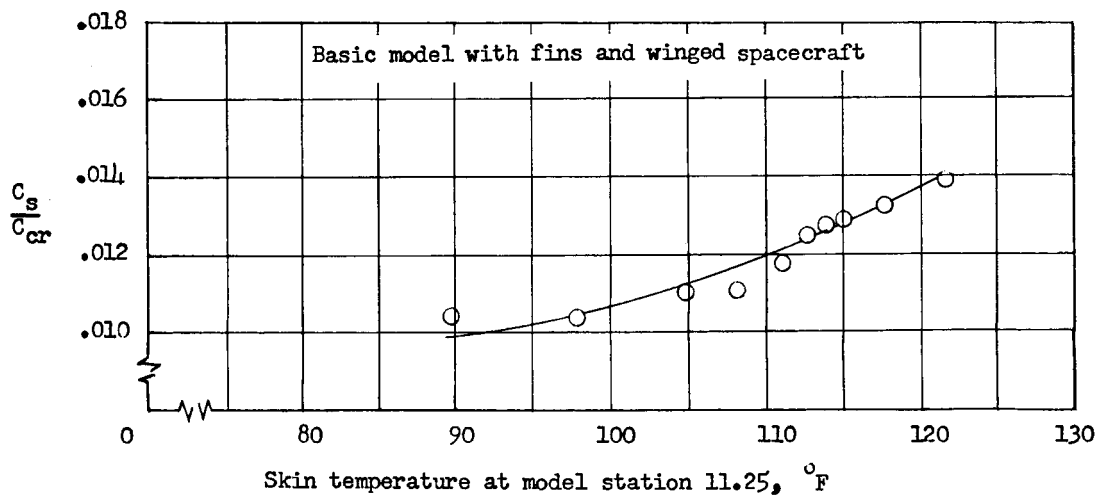
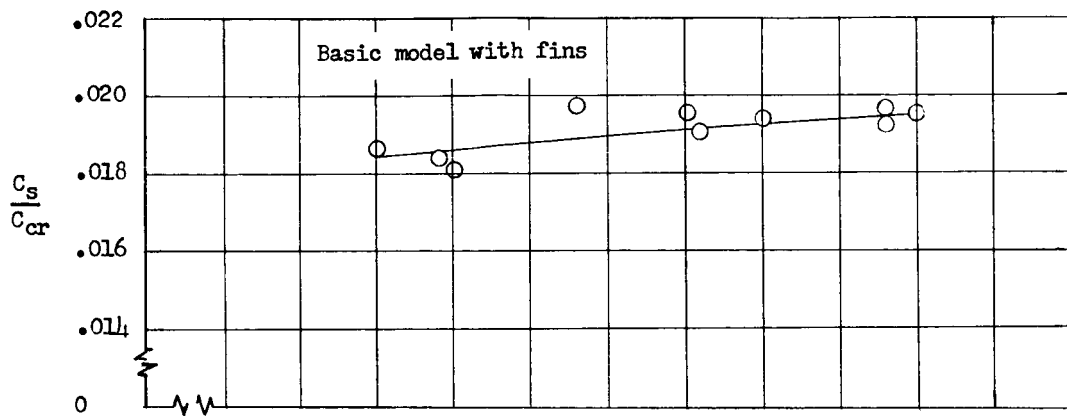
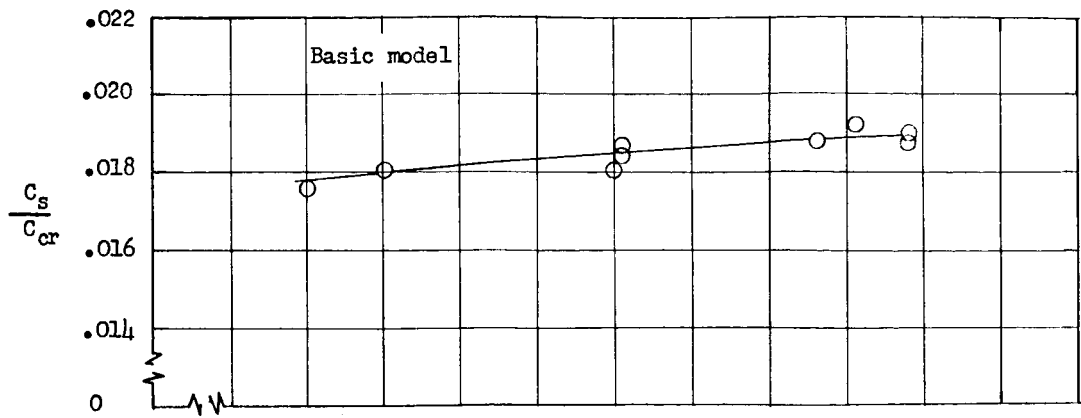


Figure 7.- Variation of structural damping with model skin temperature.

Let

$$\frac{C_A}{C_{cr}} = \frac{\pi \rho V r_r^2}{2 M_s \omega} C_h \int_0^{L/r_r} \left[ \frac{r\left(\frac{x}{r_r}\right)}{r_r} \right] H^2\left(\frac{x}{r_r}\right) d\left(\frac{x}{r_r}\right) \quad (3)$$

so that

$$C_h = \frac{\int_0^{L/r_r} c_{n\alpha} \left[ \frac{r\left(\frac{x}{r_r}\right)}{r_r} \right] H^2\left(\frac{x}{r_r}\right) d\left(\frac{x}{r_r}\right)}{\int_0^{L/r_r} \left[ \frac{r\left(\frac{x}{r_r}\right)}{r_r} \right] H^2\left(\frac{x}{r_r}\right) d\left(\frac{x}{r_r}\right)} \quad (4)$$

Thus,  $C_h$  represents an average value of  $c_{n\alpha}$  with respect to the mode shape and geometry. If equation (3) is rewritten in terms of conventional flutter parameters,

$$C_h = 2k\mu \frac{C_A}{C_{cr}} \quad (5)$$

where

$k$  reduced frequency,  $\omega L/V$

$\mu$  an effective mass ratio,  $\frac{M_s}{\pi \rho r_r^2 L \int_0^{L/r_r} \left[ \frac{r\left(\frac{x}{r_r}\right)}{r_r} \right] H^2\left(\frac{x}{r_r}\right) d\left(\frac{x}{r_r}\right)}$  where

$\int_0^{L/r_r} \left[ \frac{r\left(\frac{x}{r_r}\right)}{r_r} \right] H^2\left(\frac{x}{r_r}\right) d\left(\frac{x}{r_r}\right)$  is equal to 1.763, 1.718, and 2.41 for the basic model, basic model with fins, and basic model with fins and lifting spacecraft, respectively. The model radius function  $r\left(\frac{x}{r_r}\right)$  does not include the fins or lifting spacecraft wings.

$V$  flow velocity

$r_r$  reference radius, 0.214 ft

$\rho$  mass density of test medium

$L$  overall length of configuration

$\omega$  frequency of vibration in mode of interest

- $M_S$  generalized mass of configuration in vibration mode of interest
- $H\left(\frac{x}{r_r}\right)$  normalized mode shape
- $r\left(\frac{x}{r_r}\right)$  function which describes shape of body and specifically defined herein as local radius of body excluding any winged surfaces.

This damping-force derivative  $C_h$  is useful in scaling model results to equivalent full-scale conditions and is used in the presentation of the results of the investigation along with the damping ratio  $\frac{C_A + C_S}{C_{cr}}$ . This derivative  $C_h$ , as defined herein, differs from that in reference 1 in that the denominator of the effective mass ratio  $\mu$  has been multiplied by

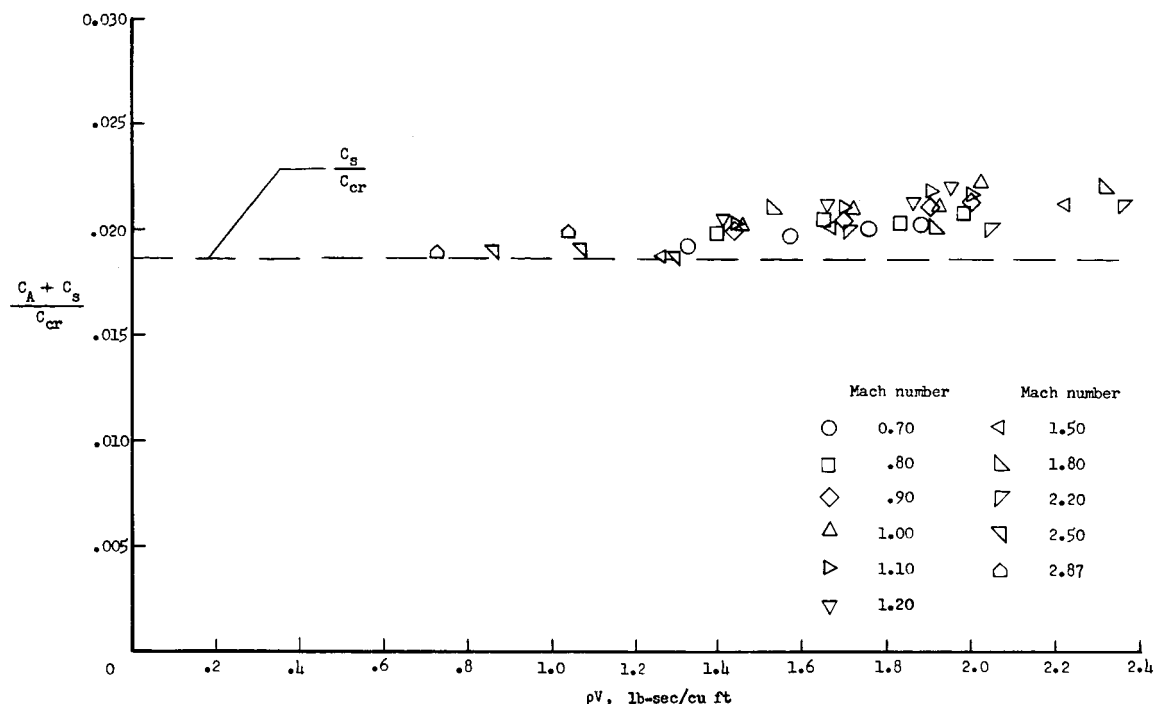
$$\int_0^{L/r_r} \left[ \frac{r\left(\frac{x}{r_r}\right)}{r_r} \right] H^2\left(\frac{x}{r_r}\right) d\left(\frac{x}{r_r}\right)$$

thus, it is "weighted" with respect to the body shape and the square of the mode shape. It is felt that this is a more logical definition of  $\mu$  since the numerator is the generalized mass (which contains the square of the mode shape) instead of the physical mass of the configuration.

## RESULTS AND DISCUSSION

The values of damping measured in this investigation for the various model configurations and test conditions are shown in figures 8 and 9. Shown in figure 8 is the variation of the ratio of total damping to critical damping with the flow parameter  $\rho V$  (test-section air density multiplied by the free-stream velocity) for the three model configurations oscillating in the first free-free bending mode at several Mach numbers. The parameter  $\rho V$  is used because theoretical approaches predict a linear variation of aerodynamic damping  $C_A$  with  $\rho V$  for a given Mach number. (See the appendix.)

The dashed line is the average structural damping ratio. Although there is scatter in the data, some observations can be made. Note that in figure 8(a) the aerodynamic damping measured on the basic model configuration is very small, being on the order of 20 percent of the structural damping ratio at the maximum  $\rho V$  tested. The absolute value of the maximum aerodynamic damping ratio is the same order of magnitude as was measured on the simpler blunt cone-cylinder model used in reference 1. The structural damping ratio of the basic model in the present investigation was approximately two times that of the full-scale vehicle. The magnitude of aerodynamic damping in the first flexible mode that the full-scale vehicle would experience along its trajectory can be estimated by using average values of the aerodynamic damping derivative  $C_h$  which will be presented later.



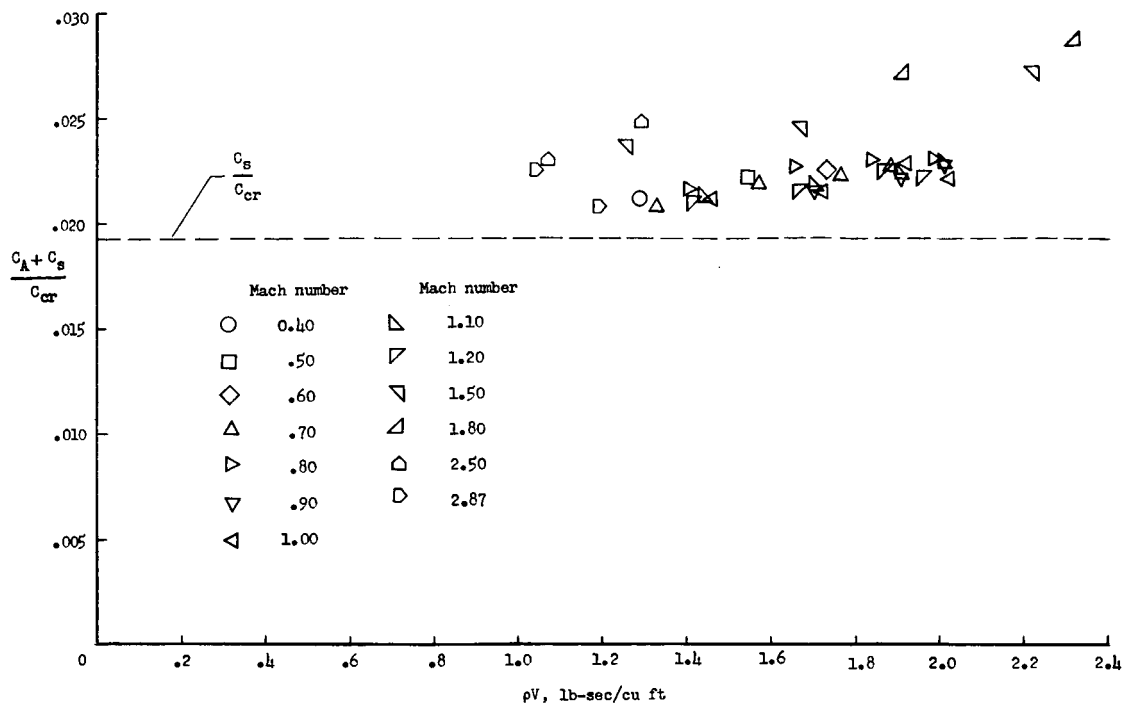
(a) Basic model.

Figure 8.- Variation of total damping ratio with flow parameter.

The effects on the total damping ratio of adding fins to the rear of the basic model and of adding fins to the rear and a winged spacecraft to the nose are shown in figures 8(b) and 8(c), respectively. The addition of the winged spacecraft to the basic model with fins changed the mode shape, generalized mass, and structural damping ratio of the basic model configuration (table I and fig. 5) so that the total damping ratios of the two configurations are not directly comparable.

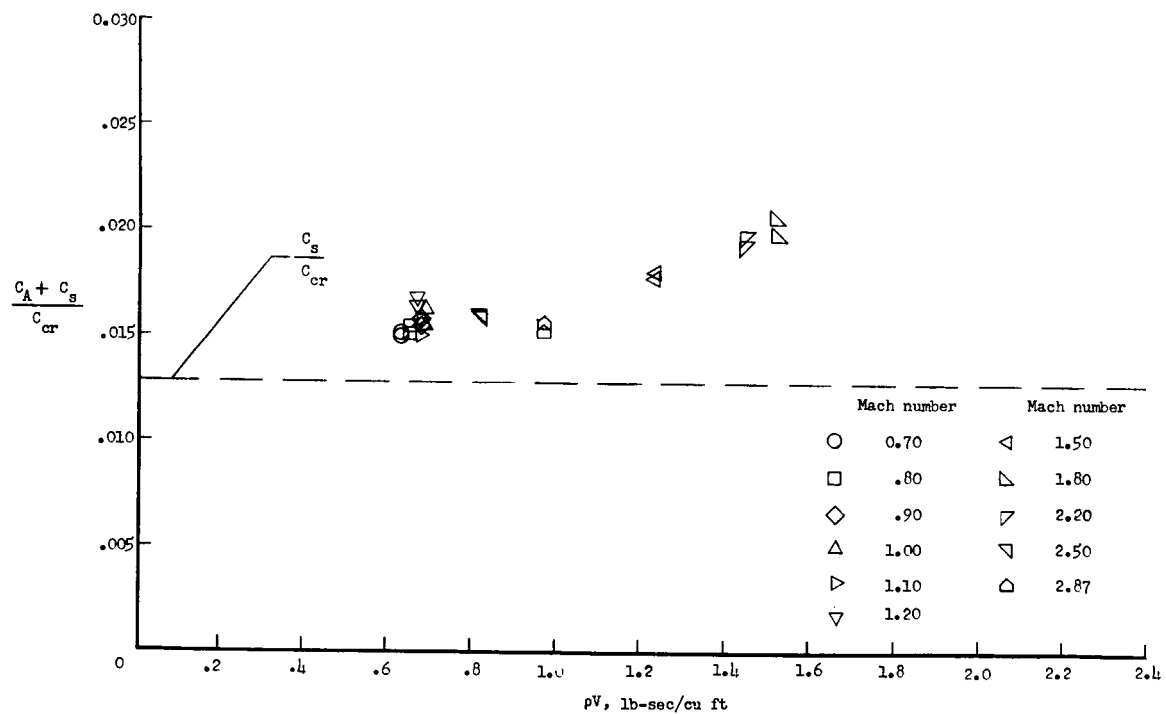
In figure 9 the aerodynamic damping derivative  $C_h$  for the first free-free vibration mode of all three model configurations is plotted against Mach number. Generally, a more pronounced Mach number effect on  $C_h$  occurred than was observed for the simpler blunt cone-cylinder model of reference 1.

Also shown in figure 9 are some aerodynamic damping derivatives calculated from several theoretical approaches (see the appendix for an explanation of how these various theories were applied) and some values for the basic model obtained from quasi-steady calculations based on static pressure-distribution measurements made on a rigid model of similar geometry.



(b) Basic model with fins.

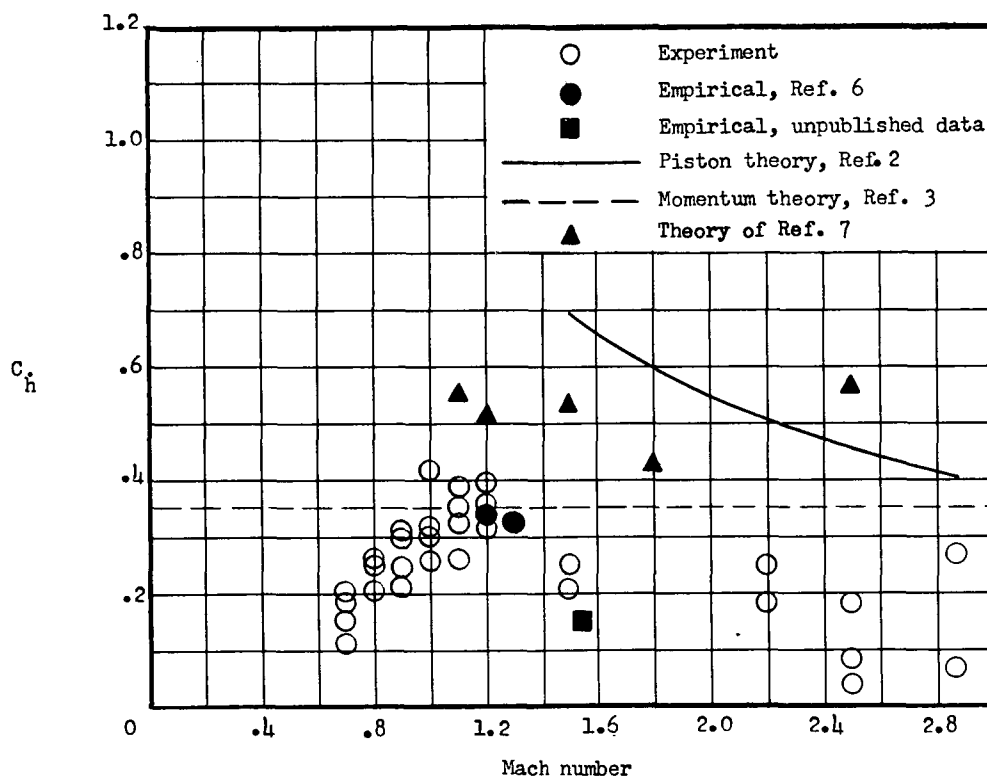
Figure 8.- Continued.



(c) Basic model with fins and winged spacecraft.

Figure 8.- Concluded.

From figure 9(a) it may be seen that for the basic model the momentum-theory values approximate the experimental values of  $C_h$ , although they are somewhat higher and the trend of the experimental results is not followed. Piston-theory values, although higher than experimental values, do indicate the general trend in the variation of  $C_h$  with Mach number. The analysis of reference 7 was applied by the staff at the Ames Research Center to calculate damping derivatives for the basic model configuration only. This analysis also gives values that are high with respect to the experimental values but predicts a less-pronounced Mach number effect than does piston theory. At Mach numbers 1.2 and 1.3, values of  $C_h$  obtained from quasi-steady calculations based on the static pressure distribution measurements on a rigid model (ref. 6) and on some similar unpublished measurements made at Mach number 1.57 agree well with the experimental results.

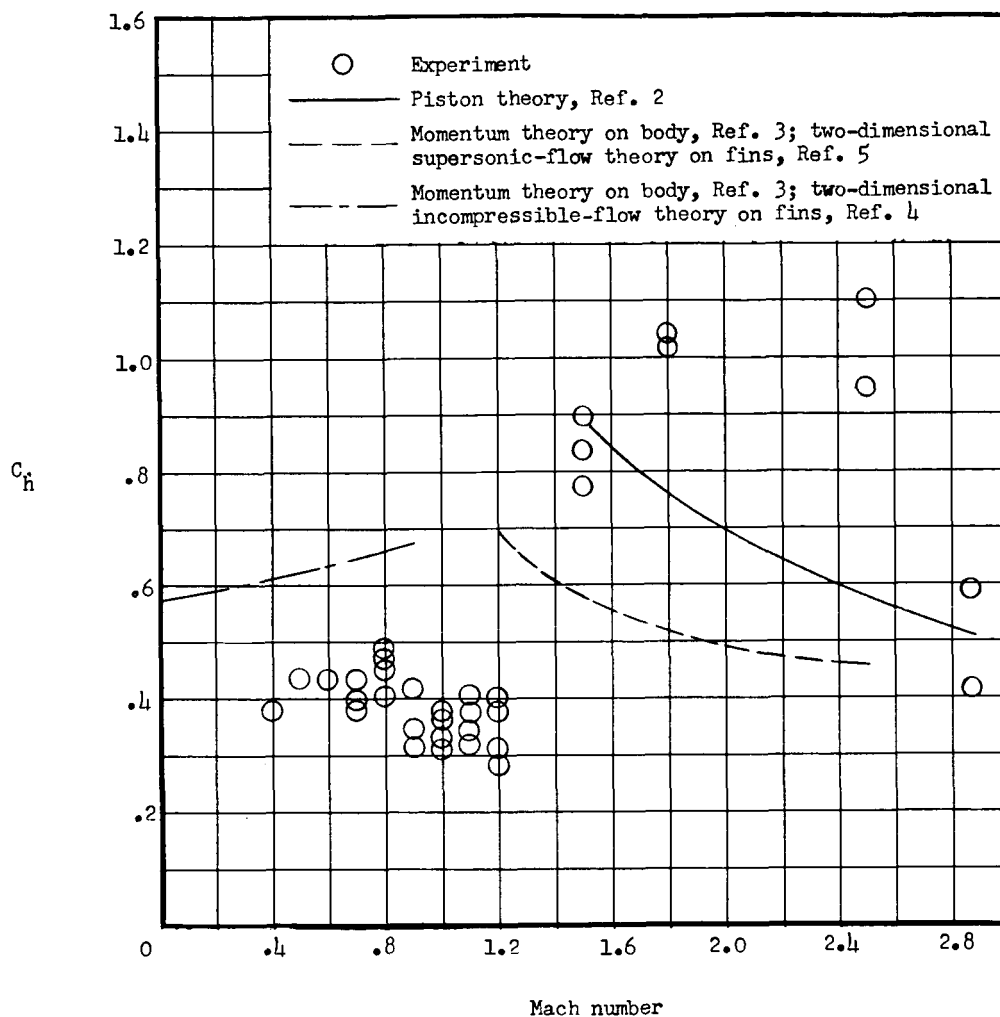


(a) Basic model.

Figure 9.- Variation of aerodynamic damping derivative with Mach number.

$$C_h = 2\mu k \frac{C_A}{C_{cr}}$$

A comparison of experimental and theoretical values of the aerodynamic damping derivative  $C_h$  for the model with fins is shown in figure 9(b). Both piston theory and momentum theory with two-dimensional supersonic flow theory of reference 5 used on fins predict the increased values of  $C_h$  that occurred with



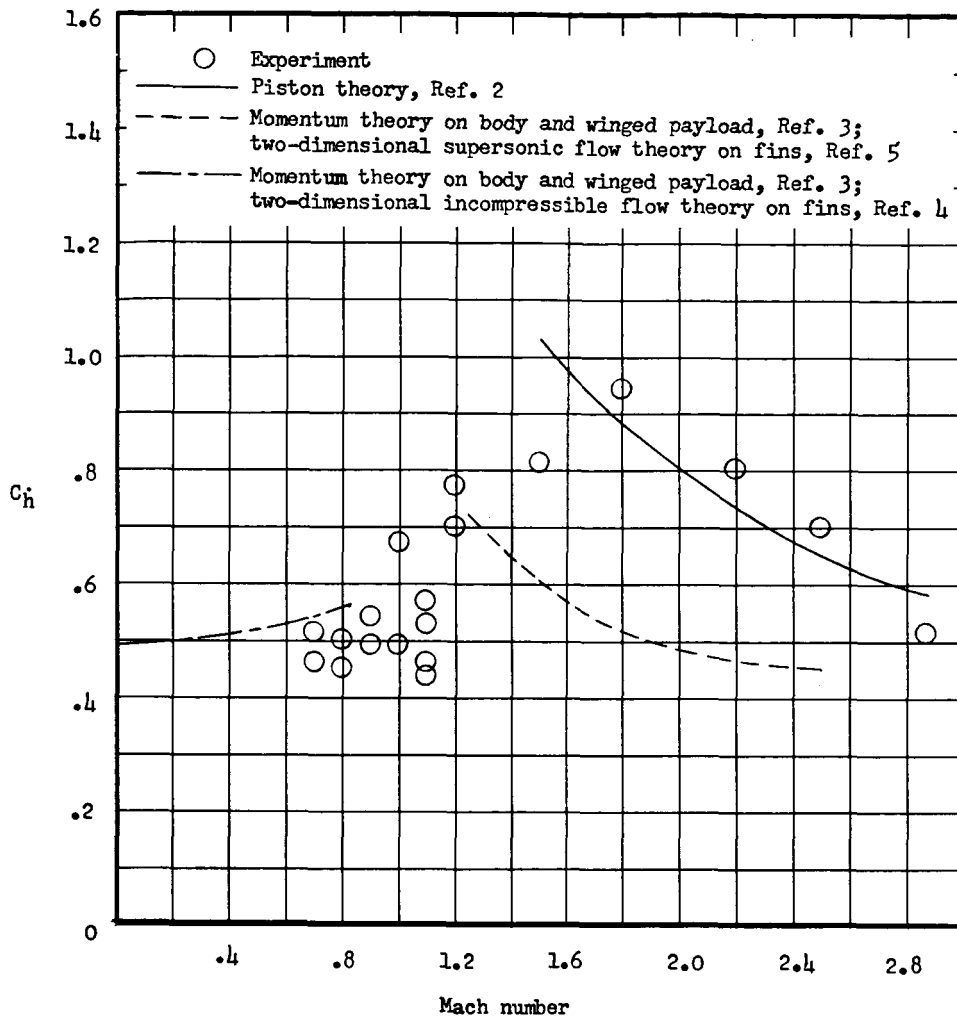
(b) Basic model with fins.

Figure 9.- Continued.

the addition of the fins over most of the supersonic Mach number range although to a lesser extent than was measured experimentally. However, the calculated and experimental trends do not agree. The effect of including fins in the momentum-theory calculations for subsonic flow with two-dimensional incompressible-flow theory of reference 4 used on fins was to raise the values of  $C_h$  considerably, and although the experimental values at subsonic speeds were also raised by the addition of the fins the calculated values were still approximately 50 percent greater than the experimental values.

In figure 9(c), which presents the results of the investigation of the basic model with fins and a winged spacecraft, piston-theory results are in good agreement with both the magnitude and the trend of the variation of  $C_h$  with Mach





(c) Basic model with fins and winged spacecraft.

Figure 9.- Concluded.

number over the applicable range although slightly low. Subsonically, momentum-theory results agree very well with the experimental results.

The effect on the aerodynamic damping derivative  $C_h$  of adding fins, and of adding both fins and a winged spacecraft to the basic model are compared in figure 10. The variation of  $C_h$  with Mach number for each configuration presented in this figure was obtained by averaging the experimental values shown at each Mach number in figure 9. From figure 10 it is seen that the addition of fins to the basic model slightly increased the aerodynamic damping derivative at Mach numbers below 1.0 and greatly increased it at the higher Mach numbers. The net effect of adding the winged spacecraft to the basic model with fins (resulting in a mode

shape change) was to raise the values of  $C_h$  slightly in the transonic speed range and to lower them in the higher Mach number range.

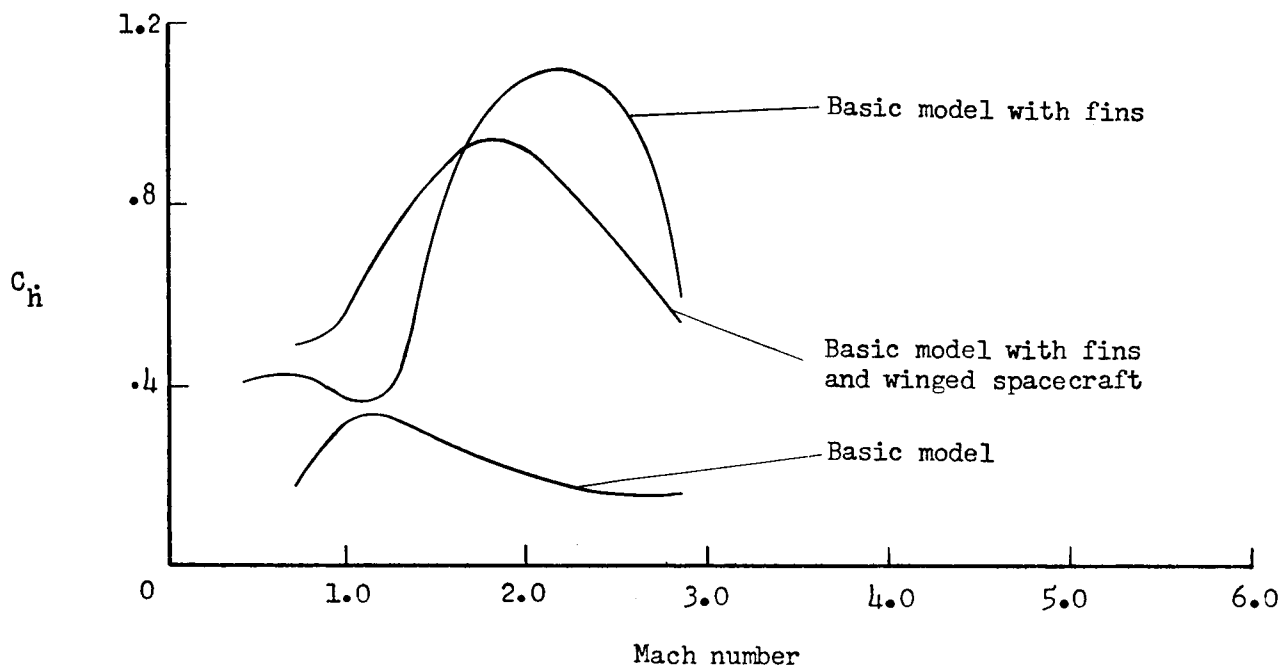


Figure 10.- Effect of configuration changes on the variation of the aerodynamic damping derivative with Mach number.

As mentioned previously, the aerodynamic damping derivative  $C_h$  can be used to obtain an estimate of the aerodynamic damping that the full-scale vehicle would experience along its trajectory. The trajectory used in the design of the model was used to obtain the variation of  $\rho V$  with Mach number. The frequency variation with Mach number was estimated from full-scale shake tests which varied booster mass distribution to account for the burning of the propellant. An estimate of the full-scale generalized mass at  $N_{Ma} = 1.2$  was obtained by scaling up the generalized mass of the model using the model-to-vehicle weight ratio. It was assumed that the mode shape of the model was the same as the mode shape of the full-scale vehicle, that it did not change with Mach number, and that the generalized mass at Mach numbers other than 1.2 varied inversely with the square of the ratio of the frequency at that Mach number to the frequency at  $N_{Ma} = 1.2$ . The variation of these parameters with Mach number is shown in figure 11. With the use of average experimentally determined values of  $C_h$  at each Mach number from figure 9(a), the ratio of aerodynamic damping to critical damping for the full-scale vehicle was calculated and plotted against Mach number in figure 12. From this figure it is seen that the maximum aerodynamic damping along the trajectory occurs at about  $N_{Ma} = 1.2$  (maximum dynamic pressure occurred at  $N_{Ma} = 1.3$  for the trajectory used) and is small. The maximum value of aerodynamic damping is less than 0.3 percent of critical damping.

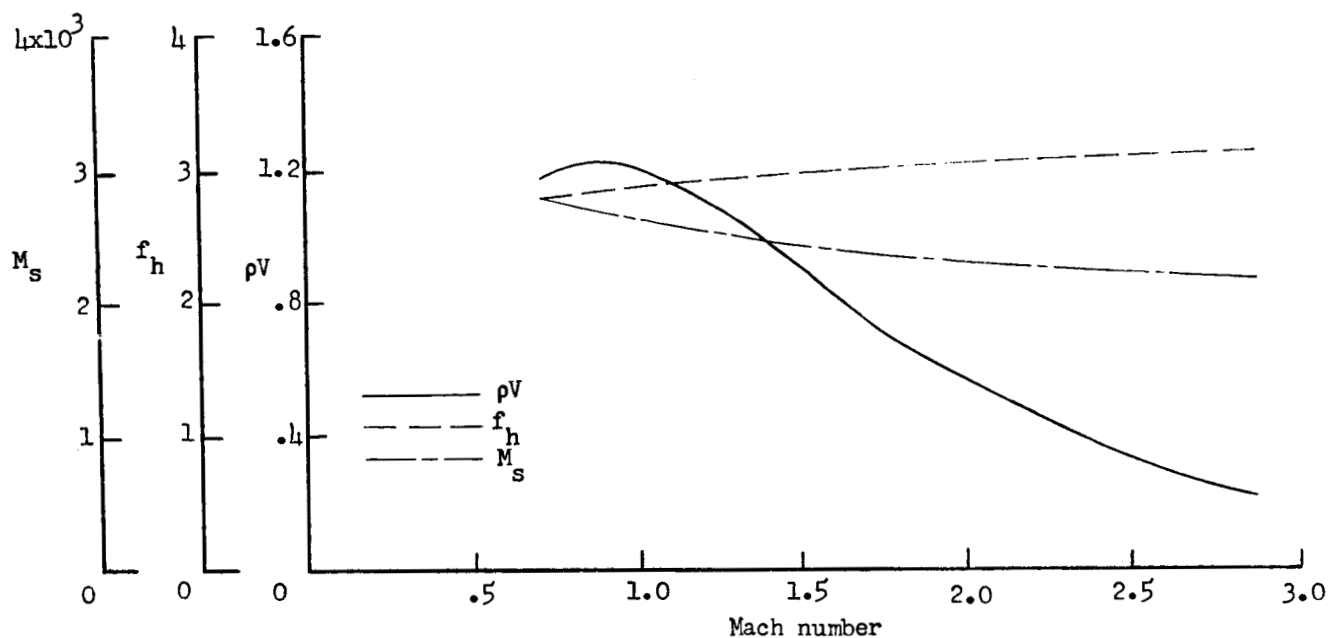


Figure 11.- Assumed full-scale values of generalized mass, frequency and density-velocity parameter for a typical Saturn SA-1 trajectory.

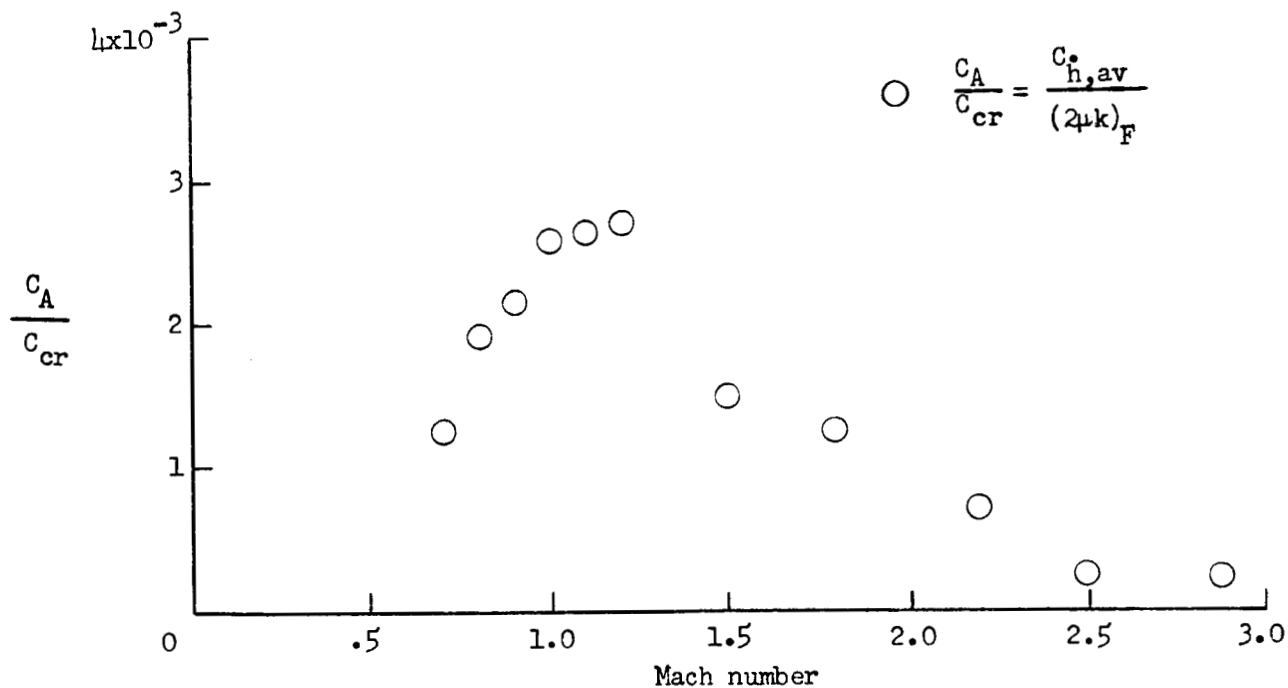


Figure 12.- Variation with Mach number of the ratio of aerodynamic damping to critical damping for the first flexible mode for a full-scale Saturn SA-1.

Although an attempt was made to measure aerodynamic stiffness in addition to aerodynamic damping in the elastic modes, as was the case for the simpler models tested in reference 1, no discernible change in model frequency was apparent outside the normal scatter in the data between the wind-off and the various tunnel wind-on conditions. (Wind-on frequency determination was accurate only to approximately 1 percent.)

As mentioned previously, hoop modes appearing in the free-free bending modes higher than the first precluded testing in these vibration modes and coupling between the rigid-body pitch and sting motions prevented the obtaining of any useful data on aerodynamic damping and stiffness in the rigid-body pitch mode of vibration.

#### CONCLUDING REMARKS

Aerodynamic damping measurements made on a flexibly mounted 0.02-scale aeroelastic model of the Saturn SA-1 launch vehicle, and other configurations, vibrating in the first free-free bending mode at Mach numbers from 0.70 to 2.87 indicate that the aerodynamic damping was small and stabilizing for all configurations tested. The maximum aerodynamic damping ratio measured on the basic model was about 20 percent of the structural damping ratio. The latter was about two times the full-scale value. The addition of fins at the rear of the model increased the value of aerodynamic damping measured throughout most of the Mach number range. The addition of the winged spacecraft altered the mode shape with the net result that the aerodynamic damping increased slightly in the subsonic and transonic Mach number ranges but decreased at Mach numbers above 1.5.

Aerodynamic stiffness effects were found to be small and fell within the experimental scatter since wind-on frequency determination was accurate only to approximately 1 percent.

Agreement of calculated aerodynamic damping derivatives with the experimental results was erratic. At supersonic speeds, piston theory generally gave the best agreement except that for the basic model the analysis of NASA Technical Note D-859 gave closer agreement with experimental results at the lower supersonic Mach numbers. Results of momentum-theory calculations were generally high in the subsonic range and low in the supersonic range except for the basic model where the results were slightly high throughout most of the Mach number range.

For the basic model, good agreement was obtained between the experimental results and some empirical quasi-steady calculations based on static pressure distribution measurements made on a rigid model of similar geometry.

Langley Research Center,  
National Aeronautics and Space Administration,  
Langley Station, Hampton, Va., June 14, 1963.

## APPENDIX

### CALCULATED AERODYNAMIC DAMPING COEFFICIENTS

The considerations used in applying the various theories are, for the most part, presented in appendix B of reference 1 but for completeness they are given and amplified herein.

The theoretical model used herein is made up of conical and cylindrical sections. The model is oscillating harmonically about a mean angle of attack of  $0^\circ$  in its first transverse bending mode at circular frequency  $\omega$ , with tip amplitude  $b(t)$  and normalized mode shape  $H\left(\frac{x}{r_r}\right)$ . The theoretical model differs from the experimental one in that the conical nose is assumed to be sharp and the scalloped first stage of the experimental model is assumed to be of a circular cross section with a radius (0.214 ft) such that the circular cross section just encloses the scalloped cross section. Since only the aerodynamic damping is desired, only those forces generated by the vertical velocity  $\dot{b}(t)H\left(\frac{x}{r_r}\right)$  are considered.

The generalized force associated with the aerodynamic damping is

$$Q_h = r_r^2 \int_0^{L/r_r} A H\left(\frac{x}{r_r}\right) d\frac{x}{r_r} \quad (A1)$$

where  $A$  is the distribution of the aerodynamic damping forces per unit length.

By use of a quasi-steady approach the distribution function  $A$  may be expressed as

$$A = 2q\pi \frac{r\left(\frac{x}{r_r}\right)}{r_r} c_{n\alpha} \frac{H\left(\frac{x}{r_r}\right)\dot{b}(t)}{V} \quad (A2)$$

where

$r\left(\frac{x}{r_r}\right)$  radius function which describes shape of body

$c_{n\alpha}$  section steady-stage normal-force-curve slope

$\frac{H\left(\frac{x}{r_r}\right)}{V}$  normalized angle of attack

Equation (A1) may now be written as

$$Q_h = \left[ \pi \rho V r_r^2 \int_0^{L/r_r} c_{n\alpha} \frac{r(\frac{x}{r_r})}{r_r} H^2\left(\frac{x}{r_r}\right) d\left(\frac{x}{r_r}\right) \right] \dot{b}(t) \quad (A3)$$

where the term in the brackets is  $C_A$ . In nondimensional form,

$$\frac{C_A}{C_{cr}} = \frac{\pi \rho V r_r^2}{2 M_S \omega} \int_0^{L/r_r} c_{n\alpha} \left[ \frac{r(\frac{x}{r_r})}{r_r} \right] H^2\left(\frac{x}{r_r}\right) d\left(\frac{x}{r_r}\right) \quad (A4)$$

In general, the equation for the aerodynamic damping ratio has to be integrated in several parts (conical nose, truncated conical portions, and cylindrical portions).

The expression for the section normal-force-curve slope as predicted by second-order piston theory of reference 2 is

$$c_{n\alpha} = \frac{1}{N_{Ma}} + \left( \frac{\gamma + 1}{2} \right) \tan \theta + \left( \frac{\gamma + 1}{4} \right) N_{Ma} \tan^2 \theta \quad (A5)$$

where

$\theta$  angle between sloping portions of model surface and undeflected center line in vertical plane

$\gamma$  ratio of specific heats

Another theory which lends itself readily to aerodynamic damping calculations is the linear small-aspect-ratio unsteady-flow theory given in reference 3. This theory gives the following equation for  $A$

$$A = \pi \rho V \left[ \frac{2r^2(\frac{x}{r_r})}{r_r^2} \frac{dH(\frac{x}{r_r})}{d(\frac{x}{r_r})} + \frac{2r(\frac{x}{r_r})}{r_r^2} \frac{dr(\frac{x}{r_r})}{d(\frac{x}{r_r})} H\left(\frac{x}{r_r}\right) \right] \dot{b}(t) \quad (A6)$$

The aerodynamic damping coefficient is

$$C_A = \pi \rho V r_r^2 \int_0^{L/r_r} \frac{d}{d(\frac{x}{r_r})} \left[ \frac{r^2(\frac{x}{r_r})}{r_r^2} H^2\left(\frac{x}{r_r}\right) \right] d\left(\frac{x}{r_r}\right) \quad (A7)$$

Performing the integration in equation (A7) yields a very concise expression for the aerodynamic damping, which is

$$C_A = \pi \rho V r_m^2 H^2(L) \quad (A8)$$

where

$H(L)$  value of normalized deflection shape at rear of model

$r_m$  radius of cylindrical portion of model at rear, 0.217 ft

In reference 7, an analysis based on a slender-body approximation is presented, the solution of which is obtained in a definite integral that has not been found to be integrable in closed form. Evaluation of the integral has been accomplished by numerical methods, and the computation forms have been programed for the IBM 704 electronic data processing machine for certain cases.

The analysis of reference 7 has been used by the staff of the Ames Research Center to calculate values of the damping force derivative  $C_h^*$  for the first flexible mode of the basic model configuration at some supersonic Mach numbers. The results of these calculations are presented in figure 9 along with the results of the other theoretical approaches used.

For the model configurations that had the fins and the winged spacecraft and fins, the effects of these surfaces were accounted for in the following manner: In the subsonic Mach number range, the two-dimensional incompressible-flow theory of reference 4 was used to calculate values of  $c_{n_\alpha}$  for the fins, and momentum theory was used for the body and winged spacecraft surfaces. In the supersonic Mach number range, the two-dimensional supersonic-flow theory of reference 5 was used to calculate values of  $c_{n_\alpha}$  for the fins, and momentum theory was used for the body and winged spacecraft surfaces.

In performing these calculations, the fins were assumed to be rigid with the normal force acting at the center of the area. The winged spacecraft wing surfaces were also assumed to have no spanwise variation of motion.

## REFERENCES

1. Hanson, Perry W., and Doggett, Robert V., Jr.: Wind-Tunnel Measurements of Aerodynamic Damping Derivatives of a Launch Vehicle Vibrating in Free-Free Bending Modes at Mach Numbers From 0.70 to 2.87 and Comparisons With Theory. NASA TN D-1391, 1962.
2. Miles, J. W., and Young, Dana: Generalized Missile Dynamics Analysis. III - Aerodynamics. GM-TR-0165-00360, Space Tech. Labs., The Ramo-Wooldridge Corp., Apr. 7, 1958.
3. Garrick, I. E.: Some Research on High-Speed Flutter. Third Anglo-American Aero. Conf., Sept. 4-7, 1951 (Brighton, England). R.A.S., 1952, pp. 419-446J.
4. Theodorsen, Theodore: General Theory of Aerodynamic Instability and the Mechanism of Flutter. NACA Rep. 496, 1935.
5. Garrick, I. E., and Rubinow, S. I.: Flutter and Oscillating Air-Force Calculations for an Airfoil in a Two-Dimensional Supersonic Flow. NACA Rep. 846, 1946. (Supersedes NACA TN 1158.)
6. Pearson, Albin O.: Wind-Tunnel Investigation at Transonic Speeds of the Static Aerodynamic Characteristics and Pressure Distributions of a Three-Stage Saturn Launch Vehicle. NASA TM X-738, 1963.
7. Bond, Reuben, and Packard, Barbara B.: Unsteady Aerodynamic Forces on a Slender Body of Revolution in Supersonic Flow. NASA TN D-859, 1961.